

Equilibrium models of relativistic stars with a toroidal magnetic field

J. Friebe¹ and L. Rezzolla^{1,2}

¹Max-Planck-Institut für Gravitationsphysik, Albert-Einstein-Institut, Am Mühlenberg 1, D-14476 Golm, Germany

²Department of Physics, Louisiana State University, Baton Rouge, LA 70803, USA

ABSTRACT

We have computed models of rotating relativistic stars with a toroidal magnetic field and investigated the combined effects of magnetic field and rotation on the apparent shape (i.e. the surface deformation), which could be relevant for the electromagnetic emission, and on the internal matter distribution (i.e. the quadrupole distortion), which could be relevant for the emission of gravitational waves. Using a sample of eight different cold nuclear-physics equations of state, we have computed models of maximum field strength, as well as the distortion coefficients for the surface and the quadrupolar deformations. Surprisingly, we find that non-rotating models admit arbitrary levels of magnetisation, accompanied by a growth of size and quadrupole distortion to which we could not find a limit. Rotating models, on the other hand, are subject to a mass-shedding limit at frequencies well below the corresponding ones for unmagnetised stars. Overall, the space of solutions can be split into three distinct classes for which the surface deformation and the quadrupole distortion are either: prolate and prolate, oblate and prolate, or oblate and oblate, respectively. We also derive a simple formula expressing the relativistic distortion coefficients and that allows one to compute the surface deformation and the quadrupole distortion up to significant levels of rotation and magnetisation, essentially covering all known magnetars. Such formula replaces Newtonian equivalent expressions that overestimate the quadrupole distortion by about a factor of five and are inadequate for strongly-relativistic objects like neutron stars.

Key words: gravitational waves – stars: magnetic field – stars: neutron.

1 INTRODUCTION

In addition to rapid rotation, also strong magnetic fields can introduce significant deformations in neutron stars, as shown, for instance, by Bocquet et al. (1995) and Cardall et al. (2001), who have computed fully nonlinear models of relativistic stars with a poloidal magnetic field. At the end of the collapse of the core of a massive star, differential rotation could create strong toroidal magnetic fields of the order of 10^{16} G – 10^{17} G inside the hot proto-neutron star (Bonazzola & Haensel 1993; Bonanno et al. 2003; Naso et al. 2008). As a result, realistic models of magnetised relativistic stars require the simultaneous presence of both poloidal and toroidal field components. As pointed out in Gourgoulhon & Bonazzola (1993), however, this requires a formalism capable of dealing with non-circular spacetimes (i.e. with convective currents in the meridional planes) like the one presented here, but which has so far been implemented only in a perturbative scheme (Ioka & Sasaki 2003, 2004). Triggered also by the increasing interest in strongly-magnetised neutron stars due to their relation with soft-gamma repeaters and anomalous X-ray pulsars (Duncan & Thompson 1992; Thompson & Duncan 1996), a growing number of studies adopting perturbative techniques have appeared investigating either the field geometry and neglecting the influence of the magnetic field on

the matter distribution (Ciolfi et al. 2009), or solving the coupled Einstein-Maxwell-Euler system, from which the magnetic deformation can be calculated (Ioka & Sasaki 2004; Colaiuda et al. 2008; Ciolfi et al. 2010; Gualtieri et al. 2011; Yoshida et al. 2012). Until recently, however, fully nonlinear models of relativistic magnetised stars were restricted to purely poloidal magnetic fields (Bocquet et al. 1995; Cardall et al. 2001), for which the generated spacetime is circular like in the unmagnetised case (Carter 1973). Following the recent insight that also a magnetic field with only a toroidal component is compatible with the circularity of spacetime (Oron 2002), studies of relativistic models of rotating stars with a toroidal magnetic field have emerged (Friebe & Rezzolla 2007; Kiuchi & Yoshida 2008; Kiuchi et al. 2009; Yasutake et al. 2010, 2011). These new studies have complemented earlier Newtonian investigations (Sinha 1968; Sood & Trehan 1972; Mikesinac 1973), which being simpler, allowed for the investigation of more complex field geometries, in particular of mixed poloidal and toroidal magnetic fields (Tomimura & Eriguchi 2005; Yoshida et al. 2006; Haskell et al. 2008; Lander & Jones 2009; Fujisawa et al. 2012).

In this work, we are mainly concerned with the deformation of neutron stars endowed with a toroidal magnetic field because they might be an important source of gravitational radiation due to the prolate deformation induced by the magnetic field and provided

arXiv:1207.4035v1 [gr-qc] 17 Jul 2012

that the axes of symmetry and of rotation are different (Bonazzola & Gourgoulhon 1996). Furthermore, Jones (1975) has pointed out that viscous processes can trigger a secular instability, which drives the axis of symmetry of the prolate star into the plane perpendicular to the angular momentum vector transforming it into a bar-shaped rotating source of gravitational radiation (Cutler 2002; Stella et al. 2005). From the astrophysical point of view, both the deformation of the stellar surface as well as the distortion of the matter distribution are relevant and can be measured by appropriate quantities, namely the surface deformation (or apparent oblateness) and the quadrupole distortion. Previous studies of relativistic models of stars with a toroidal magnetic field have provided a broad survey of nonrotating and rotating models for varying masses, radii and magnetic fluxes. The focus of this work is a complementary one to earlier studies: in order to obtain a comprehensive picture of the impact of a toroidal magnetic field on relativistic stars, we exclusively study models of fixed baryon mass corresponding to a gravitational mass of $M = 1.400 M_{\odot}$ in the unmagnetised and nonrotating case. Although we expect neutron stars to come in a narrow but nonzero range of masses, restricting to a single value of the gravitational mass has the important advantage that we can explore with unprecedented precision both the deformations introduced by magnetic fields and those introduced by rapid rotation. As we will comment later on, our increased accuracy has allowed us also to discover novel results and equilibrium configurations.

Our neutron stars are modelled assuming the matter to be a perfect fluid well described by a single-parameter equation of state (EOS), and as having infinite conductivity, as required by the ideal magneto-hydrodynamics (MHD) limit. We do not consider multi-fluid models, which would allow for the stratification of neutron-star matter, nor do we treat the protons in the interior as a superconducting fluid, which would greatly alter the magnetic properties of associated equilibrium models. Nevertheless, important results obtained for extremely magnetised models with field strengths of the order of 10^{17} G can be readily extended to configurations of much lower and more realistic field strengths of the order of 10^{13} G. More specifically, in addition to a standard $\gamma = 2$ polytropic EOS, we have considered a sample of seven realistic EOSs resulting from calculations of cold catalysed dense matter, namely the APR EOS (Akmal et al. 1998), the BBB2 EOS (Baldo et al. 1997), the BN1H1 EOS (Balberg & Gal 1997), the BPAL12 EOS (Bombaci 1995), the FPS EOS (Pandharipande & Ravenhall 1989), the GNH3 EOS (Glendenning 1985) and the SLy4 EOS (Douchin & Haensel 2001). Altogether, this set of EOSs spans a wide range of physical properties and should cover any realistic description of neutron stars. For the Pol2 EOS, we have explored systematically the space of solutions and computed the corresponding surface deformation and quadrupole distortion. In addition, we have also computed the distortion coefficients, which allow one to compute the deformation of neutron stars up to large magnetizations and rotation rates through a simple algebraic expression, following the procedure devised in Cutler (2002).

The plan of the article is the following: in Sect. 2, we give an overview of the novel results obtained in this study, in Sect. 3, we discuss the theoretical framework on which our approach, whose numerical implementation and testing is discussed in Sect. 4, is based. Results for static magnetised models are presented in Sect. 5 and for rotating magnetised models in Sect. 6. In Sect. 7, we deal with the case of moderate magnetic field and rotation and derive empirical distortion coefficients before presenting our conclusions in Sect. 8.

2 OVERVIEW OF THE MAIN RESULTS

Given the complexity of the numerous results found and the risk that the most important ones may be lost in the details, in the following we briefly summarise what we believe are the most salient results obtained. We recall that we measure with ϵ_s the deformation of the surface shape, while we measure with ϵ the (quadrupolar) deviation of the matter distribution from a spherically symmetric one. Overall, equilibrium models of relativistic stars with a toroidal magnetic field exhibit the following properties:

- *nonrotating* and *magnetised* models exhibit a prolate surface deformation and a prolate quadrupolar deformation, i.e. $\epsilon_s < 0$, $\epsilon < 0$, both of which decrease as the magnetisation parameter λ_0 is increased.
- *rotating* and *unmagnetised* models exhibit an oblate surface deformation and an oblate quadrupolar deformation, i.e. $\epsilon_s > 0$, $\epsilon > 0$, both of which increase as the rotation frequency is increased.
- between these limiting cases, neutral lines $\epsilon_s = 0$ and $\epsilon = 0$ divide models into having prolate/oblate surface deformations and prolate/oblate internal deformations, respectively.
- for *nonrotating* models no upper limit was found to the magnetisation parameter λ_0 , with stellar models that become increasingly prolate, but also increasingly extended as the magnetisation is increased [see Figs. 6 and 7].
- the magnetic pressure associated with the toroidal magnetic field also causes an expansion in the outer layers of the star, in particular a growth of its equatorial radius. This effect is present also for nonrotating models, for which, however, the polar radius grows more rapidly than the equatorial one, yielding a prolate surface deformation, i.e. $\epsilon_s < 0$. However, as the rotation is increased and the magnetisation decreased, models can be found which have a prolate interior deformation, i.e. $\epsilon < 0$, and an oblate surface deformation, i.e. $\epsilon_s > 0$.
- for any given angular velocity, the model of maximum magnetisation coincides with the mass-shedding model, i.e. the model for which centrifugal and gravitational forces are equal at the equatorial radius. This point is characterized by the appearance of a cusp at the equator.
- for *rotating* models the magnetic pressure at the equator adds to the centrifugal force, favouring the loss of mass. As a result of the increase in the equatorial size, the mass-shedding frequency is systematically smaller than the corresponding one for unmagnetised models.
- in the space of parameters considered, the average toroidal magnetic-field strength $\langle B^2 \rangle^{1/2}$ is not a monotonic function of the intrinsic magnetisation parameter λ_0 , and after reaching a maximum value, it gradually decreases. This implies the existence of double solutions in certain parts of the space of parameters $(\Omega^2, \langle B^2 \rangle)$.
- although the space of parameters $(\Omega^2, \langle B^2 \rangle)$ is potentially degenerate, the corresponding space of parameters (Ω^2, λ_0^2) is not. As a result, any stellar model considered is characterised uniquely by the values of the angular velocity Ω and of the magnetisation parameter λ_0 .

Given these results, it is natural to divide our models into three classes: (1) models labelled PP for prolate-prolate, for which both apparent shape and matter distribution are prolate, i.e. $\epsilon_s < 0$, $\epsilon < 0$; (2) models labelled PO for prolate-oblate, whose shape is oblate whereas their matter distribution is prolate, i.e. $\epsilon_s > 0$, $\epsilon < 0$; (3) models labelled OO for oblate-oblate, which appear oblate and also exhibit an oblate matter distribution; i.e. $\epsilon_s > 0$, $\epsilon > 0$. The latter

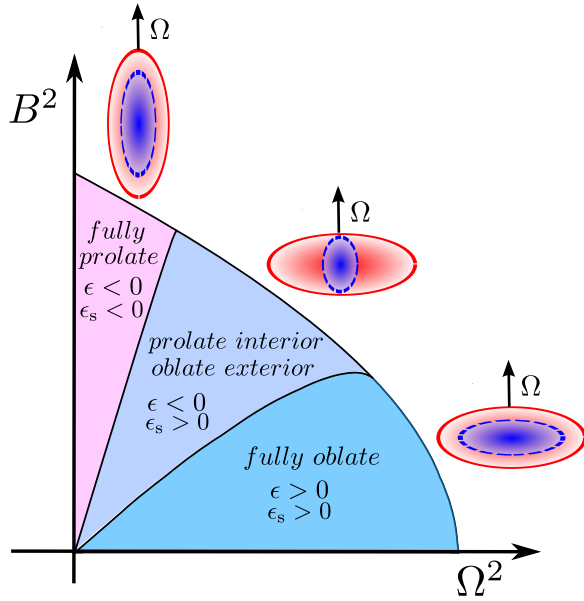


Figure 1. Schematic diagram showing the space of solutions of equilibrium models in the (Ω^2, B^2) plane. According to the relative strength of the magnetic field and of the rotation rate, different combinations of the surface deformation, ϵ_s , and of the quadrupole deformation, ϵ , are possible.

class of models had not been found by Kiuchi & Yoshida (2008). A schematic picture illustrating the three different classes is shown in Fig. 1. Finally, while different EOSs with their different stiffness introduce quantitative differences in the behaviour described above, they all follow the same qualitative behaviour.

3 MATHEMATICAL AND NUMERICAL SETUP

3.1 Basic assumptions

We assume that the spacetime generated by the rotating star is *stationary* and *axisymmetric*, with Killing vector fields e_0 and e_3 associated with these symmetries. If, in addition, the spacetime is asymptotically flat and there exists an axis where e_3 vanishes, then e_0 and e_3 commute (Carter 1970). This enables us to choose coordinates $(x^\alpha) = (t, r, \theta, \phi)$ with vector fields $e_0 = \partial/\partial t$ and $e_3 = \partial/\partial \phi$. If furthermore the total stress-energy tensor T satisfies the *circularity* conditions

$$T \cdot e_0 = \alpha e_0 + \beta e_3, \quad (1)$$

$$T \cdot e_3 = \lambda e_0 + \mu e_3, \quad (2)$$

convective currents in the meridional planes of constant (t, ϕ) are absent by construction. In this case, quasi-isotropic (QI) coordinates can be adopted and the line element reads

$$ds^2 = g_{\alpha\beta} dx^\alpha dx^\beta = -N^2 dt^2 + \Phi^2 r^2 \sin^2 \theta (d\phi - N^\phi dt)^2 + \Psi^2 (dr^2 + r^2 d\theta^2). \quad (3)$$

where N , N^ϕ , Ψ , and Φ are functions of (r, θ) . We further introduce the Eulerian observer O_0 whose four-velocity n is the future-directed unit-vector normal to hypersurfaces of constant t . From Eq. (3), we infer $n_\alpha = (-N, 0, 0, 0)$.

The compatibility of the electromagnetic fields with the circularity condition was established long ago (Carter 1973) for the case in which the electromagnetic-field tensor F is derived from a potential 1-form A with components $(A_r, 0, 0, A_\phi)$, whereas the

contravariant components of the electric current vector j read $j^\alpha = (j^t, 0, 0, j^\phi)$. This fact has been exploited for computing fully relativistic models of stars with a poloidal electromagnetic field (Bocquet et al. 1995; Cardall et al. 2001). However, it has been shown that the case of a toroidal magnetic field satisfies the circularity assumption, too (Oron 2002; Kiuchi & Yoshida 2008). In the following, we adopt a vector potential which is orthogonal to the Killing vectors e_0 and e_3 , namely $A \cdot e_0 = 0$ and $A \cdot e_3 = 0$. The covariant components of A then become

$$A_\alpha = (0, A_r, A_\theta, 0). \quad (4)$$

This particular form of A ensures, by construction, the absence of any poloidal electric or magnetic-field component. The only non-vanishing component of the antisymmetric Faraday tensor $F_{\alpha\beta} = A_{\beta,\alpha} - A_{\alpha,\beta}$ is then given by

$$F_{r\theta} = \frac{\partial A_\theta}{\partial r} - \frac{\partial A_r}{\partial \theta}. \quad (5)$$

For the *electric field* E and the *magnetic field* B as measured by observer O_0 , we then obtain

$$E_\alpha = F_{\alpha\beta} n^\beta = (0, 0, 0, 0), \quad (6)$$

$$B_\alpha = -\frac{1}{2} \eta_{\alpha\beta\gamma\delta} F^{\gamma\delta} n^\beta = \frac{\Phi \sin \theta}{\Psi^2} \left(N^\phi \left[\frac{\partial A_r}{\partial \theta} - \frac{\partial A_\theta}{\partial r} \right], 0, 0, - \left[\frac{\partial A_r}{\partial \theta} - \frac{\partial A_\theta}{\partial r} \right] \right), \quad (7)$$

where $\eta_{\alpha\beta\gamma\delta}$ is the totally antisymmetric tensor associated with the metric g . According to Eqs. (6) and (7), the combination of a vanishing electric field and of a toroidal magnetic field holds for *any* observer whose 4-velocity u is a linear combination of the two Killing vectors e_0 and e_3 . The electromagnetic contribution to the stress energy tensor is given by

$$\mathcal{T}_{\alpha\beta} = \frac{1}{4\pi} \left(F_{\alpha\kappa} F^\kappa_\beta - \frac{1}{4} F_{\kappa\lambda} F^{\kappa\lambda} g_{\alpha\beta} \right). \quad (8)$$

Following the procedure adopted by Bonazzola et al. (1993), \mathcal{T} is split up into the total electromagnetic energy density \mathcal{E} , the Poynting 3-vector \mathcal{J} , and the electromagnetic stress 3-tensor \mathcal{S} as measured by the Eulerian observer O_0 . With the projection tensor $h = g + n \otimes n$, these quantities are obtained as projections of \mathcal{T} onto and orthogonal to n , namely $\mathcal{E} \equiv n \cdot \mathcal{T} \cdot n$, $\mathcal{J} \equiv -h \cdot \mathcal{T} \cdot n$, and $\mathcal{S} \equiv h \cdot \mathcal{T} \cdot h$. Specialised to the present case of no electric field and no poloidal magnetic-field components, the electromagnetic contribution to the (3+1) matter variables (for an introduction to the (3+1) formalism of general relativity, cf. Smarr & York 1978;ourgoulhon 2012), namely the total energy density $E \equiv n \cdot T \cdot n$, the momentum density 3-vector $J \equiv -h \cdot T \cdot n$, and the stress 3-tensor $S \equiv h \cdot T \cdot h$ reads

$$\mathcal{E} = \frac{1}{8\pi} \left(\frac{B_\phi}{\Phi r \sin \theta} \right)^2, \quad (9)$$

$$\mathcal{J}_i = 0, \quad (10)$$

$$S^r_r = \mathcal{E}, \quad S^\theta_\theta = \mathcal{E}, \quad S^\phi_\phi = -\mathcal{E}. \quad (11)$$

In particular, all non-diagonal components of S^i_j are zero, and $S = \mathcal{E}$. The circularity assumption requires that for the Poynting vector \mathcal{J}

$$\mathcal{J}_r = 0, \quad \mathcal{J}_\theta = 0, \quad (12)$$

and that the electromagnetic stress tensor \mathcal{S} satisfies

$$S_{r\phi} = 0, \quad S_{\theta\phi} = 0. \quad (13)$$

3.2 Einstein Equations

The Einstein equations for the metric tensor g defined by Eq. (3) and a general stress-energy tensor T decomposed into the (3+1) quantities E , J , and S become

$$\Delta v = 4\pi\Psi^2(E+S) + \frac{\Phi^2 r^2 \sin^2 \theta}{2N^2} (\partial N^\phi)^2 - \partial v \partial(v+\beta), \quad (14)$$

$$\tilde{\Delta}_3(N^\phi r \sin \theta) = -16\pi \frac{N\Psi^2}{\Phi^2} \frac{J_\phi}{r \sin \theta} - r \sin \theta \partial N^\phi \partial(3\beta-v), \quad (15)$$

$$\Delta_2[(N\Phi - 1) r \sin \theta] = 8\pi N\Psi^2 \Phi (S^r_r + S^\theta_\theta) r \sin \theta, \quad (16)$$

$$\Delta_2 \zeta = 8\pi\Psi^2 S^\phi_\phi + \frac{3\Phi^2 r^2 \sin^2 \theta}{4N^2} (\partial N^\phi)^2 - (\partial v)^2. \quad (17)$$

where the following abbreviations have been used

$$v \equiv \ln N, \quad \zeta \equiv \ln(N\Psi), \quad \beta \equiv \ln \Phi, \quad (18)$$

$$\Delta_2 \equiv \frac{\partial^2}{\partial r^2} + \frac{1}{r} \frac{\partial}{\partial r} + \frac{1}{r^2} \frac{\partial^2}{\partial \theta^2}, \quad (19)$$

$$\Delta_3 \equiv \frac{\partial^2}{\partial r^2} + \frac{2}{r} \frac{\partial}{\partial r} + \frac{1}{r^2} \frac{\partial^2}{\partial \theta^2} + \frac{1}{r^2 \tan \theta} \frac{\partial}{\partial \theta}, \quad (20)$$

$$\tilde{\Delta}_3 \equiv \Delta_3 - \frac{1}{r^2 \sin^2 \theta}, \quad (21)$$

$$\partial a \partial b \equiv \frac{\partial a}{\partial r} \frac{\partial b}{\partial r} + \frac{1}{r^2} \frac{\partial a}{\partial \theta} \frac{\partial b}{\partial \theta}. \quad (22)$$

The resulting system of four nonlinear elliptic equations for the metric variables N , N^ϕ , Ψ , and Φ can be solved iteratively once suitable boundary conditions of asymptotic flatness have been adopted. Additional details can be found in Bonazzola et al. (1993).

3.3 Maxwell equations

Since the electromagnetic-field tensor F is derived from a potential 1-form A , the homogeneous Maxwell equations

$$F_{\alpha\beta;\gamma} + F_{\beta\gamma;\alpha} + F_{\gamma\alpha;\beta} = 0 \quad (23)$$

are satisfied by construction. The inhomogeneous Maxwell equations $F^{\alpha\beta}_{;\beta} = 4\pi j^\alpha$ allow to express the electric current 4-vector j in terms of the Faraday tensor F , where the alternative expression

$$4\pi j^\alpha = \frac{1}{\sqrt{-g}} (\sqrt{-g} F^{\alpha\beta})_{;\beta} \quad (24)$$

with $\sqrt{-g} = \Psi^2 \Phi N r^2 \sin \theta$ is used. The electromagnetic field tensor F has only one non-vanishing contra- and covariant component, which can be now expressed in terms of the azimuthal component B_ϕ of the magnetic field B ,

$$F_{r\theta} = \frac{\Psi^2}{\Phi \sin \theta} B_\phi, \quad (25)$$

$$F^{r\theta} = \frac{B_\phi}{\Psi^2 \Phi r^2 \sin \theta}. \quad (26)$$

Combining Eqs. (24) and (25), the poloidal components of the electric current 4-vector j can be written as

$$4\pi j^r = \frac{1}{\Psi^2 \Phi N r^2 \sin \theta} \frac{\partial(NB_\phi)}{\partial \theta}, \quad (27)$$

$$4\pi j^\theta = -\frac{1}{\Psi^2 \Phi N r^2 \sin \theta} \frac{\partial(NB_\phi)}{\partial r}, \quad (28)$$

The remaining components j^i and j^ϕ are zero, as expected. Note that the circularity condition, Eqs. (1), (2), forbids any meridional convective current contributing to J , which is ensured by assuming the charge carriers to be *massless*. By taking the divergence of Eq. (24), it follows that $j^\alpha_{;\alpha} = 0$ thanks to the antisymmetry of

F , and this continuity equation for the electric current leads to a dependence between j^r and j^θ , namely

$$\nabla \cdot j = \frac{1}{\sqrt{-g}} \left[\frac{\partial}{\partial r} (\sqrt{-g} j^r) + \frac{\partial}{\partial \theta} (\sqrt{-g} j^\theta) \right] = 0, \quad (29)$$

which however is trivially fulfilled by virtue of Eqs. (27) and (28) which express j^r and j^θ as functions of a single quantity, namely, NB_ϕ , without any restriction from Eq. (29). A useful consequence of Eqs. (27) and (28) is that the flow lines of the electric current coincide with the isocontours of NB_ϕ , which allows one to visualise the current distribution without actually computing j .

3.4 Equation of motion and condition on the Lorentz force

In the case of a perfect fluid the stress energy tensor T takes the form

$$T = (e + p) u \otimes u + p g, \quad (30)$$

where e is the energy density and p the pressure as measured by the *fluid comoving observer* O_1 with 4-velocity u . Since we assume the absence of meridional currents, u can be written as a linear combination of the Killing vectors e_0 and e_3 , namely

$$u = u^t e_0 + u^\phi e_3. \quad (31)$$

Introducing the Lorentz factor $\Gamma \equiv -n \cdot u = Nu^t$ linking observers O_0 and O_1 and the fluid coordinate angular velocity $\Omega \equiv u^\phi/u^t$, the physical fluid velocity U and the Lorentz factor Γ can be expressed respectively as

$$U = \frac{\Phi r \sin \theta}{N} (\Omega - N^\phi), \quad (32)$$

$$\Gamma = (1 - U^2)^{1/2}. \quad (33)$$

Taking into account the contribution of the magnetic field to the (3+1) matter variables according to Eqs. (9)–(11), the following expressions are obtained for a perfect fluid endowed with a toroidal magnetic field,

$$E = \Gamma^2(e + p) - p + \frac{1}{8\pi} \left(\frac{B_\phi}{\Phi r \sin \theta} \right)^2, \quad (34)$$

$$J_\phi = \Gamma^2(e + p) \Phi r \sin \theta U, \quad (35)$$

$$S^r_r = S^\theta_\theta = p + \frac{1}{8\pi} \left(\frac{B_\phi}{\Phi r \sin \theta} \right)^2, \quad (36)$$

$$S^\phi_\phi = p + \Gamma^2(e + p) U^2 - \frac{1}{8\pi} \left(\frac{B_\phi}{\Phi r \sin \theta} \right)^2. \quad (37)$$

All other components are zero, and $S = 3p + \Gamma^2(e + p) U^2 + 1/(8\pi)(B_\phi/(\Phi r \sin \theta))^2$. The projection of $\nabla \cdot T = 0$ onto spatial hypersurfaces of constant t provides the equation of motion

$$\frac{1}{e + p} \frac{\partial p}{\partial x^i} + \frac{\partial v}{\partial x^i} - \frac{\partial}{\partial x^i} (\ln \Gamma) - \frac{1}{e + p} F_{i\beta} j^\beta = -F \frac{\partial \Omega}{\partial x^i}, \quad (38)$$

where F is defined as

$$F \equiv u_\phi u^t = \Gamma^2 \frac{\Phi}{N} U r \sin \theta. \quad (39)$$

Assuming a single-parameter EOS, $e = e(n)$ and $p = p(n)$, with n the baryon number density, we introduce the fluid log-enthalpy

$$H \equiv \ln \left(\frac{e + p}{n m_b} \right), \quad (40)$$

with a mean baryon rest mass of $m_b = 1.66 \times 10^{-27}$ kg. Using Eqs. (25)–(28), (40), and discarding the case of differential rotation, Eq. (38) becomes

$$\frac{\partial}{\partial x^i} (H + \nu - \ln \Gamma) + \left(\frac{1}{e+p} \right) \left(\frac{1}{8\pi \Phi^2 N^2 r^2 \sin^2 \theta} \right) \frac{\partial (NB_\phi)^2}{\partial x^i} = 0. \quad (41)$$

Equation (41) can only be satisfied if the Lorentz force term is derived from a scalar function $\tilde{M}(r, \theta)$ as well, thus we require

$$\left(\frac{1}{e+p} \right) \left(\frac{1}{8\pi \Phi^2 N^2 r^2 \sin^2 \theta} \right) \frac{\partial (NB_\phi)^2}{\partial x^i} = \frac{\partial \tilde{M}}{\partial x^i}. \quad (42)$$

Using the Schwartz theorem, the integrability condition of Eq. (42) can be written as

$$\frac{\partial G}{\partial \theta} \frac{\partial (NB_\phi)}{\partial r} - \frac{\partial G}{\partial r} \frac{\partial (NB_\phi)}{\partial \theta} = 0, \quad (43)$$

where $G \equiv (e+p)\Phi^2 N^2 r^2 \sin^2 \theta$. In other words, Eq. (43) states that the Jacobian of the coordinate transform $(r, \theta) \rightarrow (G, NB_\phi)$ is zero, and hence there exists a scalar function $\Theta : \mathbf{R}^2 \rightarrow \mathbf{R}$ such that $\Theta(G, NB_\phi) = 0$. Two different cases can be distinguished: (i) If $\partial \Theta / \partial (NB_\phi) = 0$, then Θ does not depend on NB_ϕ , and the relation $\Theta(G, NB_\phi) = 0$ implies that G is constant, which is equivalent to the absence of any matter and $G = 0$. (ii) If $\partial \Theta / \partial (NB_\phi) \neq 0$, then the implicit-function theorem enables us to write $NB_\phi = NB_\phi(G)$. Discarding the case without matter, we retain possibility (ii) and conclude that

$$NB_\phi = g((e+p)\Phi^2 N^2 r^2 \sin^2 \theta), \quad (44)$$

with g being an arbitrary scalar function. However, the regularity properties of an axisymmetric vector field in the case of spatial spherical coordinates (r, θ, ϕ) impose some further restrictions on g . For the covariant component U_ϕ of an azimuthal vector field $\mathbf{U} = U^\phi \mathbf{e}_3$, it can be shown (Bardeen & Piran 1983) that

$$U_\phi(r, \theta) = r^2 \sin^2 \theta m(r, \theta), \quad (45)$$

where m is an arbitrary axisymmetric scalar function. Application of Eq. (45) to NB_ϕ allows to conclude that g can be written as $g(x) = xf(x)$, with an arbitrary regular scalar function f . The resulting expression for NB_ϕ after application of Eq. (45) to Eq. (44) reads

$$NB_\phi = (e+p)\Phi^2 N^2 r^2 \sin^2 \theta f((e+p)\Phi^2 N^2 r^2 \sin^2 \theta). \quad (46)$$

By inserting Eq. (46) into Eq. (42), the gradient of the magnetic potential \tilde{M} reads

$$\frac{\partial \tilde{M}}{\partial x^i} = \frac{f}{4\pi} \frac{\partial}{\partial x^i} [(e+p)\Phi^2 N^2 r^2 \sin^2 \theta f] = R_i. \quad (47)$$

In general, \tilde{M} cannot be determined in closed form. However, inspection of Eq. (47) reveals that for the sub-case of a monomial function $f(x) = \lambda_m x^m$ (not to be meant as a summation over repeated indices), a solution can be written down immediately. In this case, Eq. (46) simplifies to

$$NB_\phi = \lambda_m ((e+p)\Phi^2 N^2 r^2 \sin^2 \theta)^{m+1}, \quad (48)$$

and the solution to Eq. (47) is given by an algebraic expression, namely

$$\tilde{M} = \frac{\lambda_m^2}{4\pi} \left(\frac{m+1}{2m+1} \right) ((e+p)\Phi^2 N^2 r^2 \sin^2 \theta)^{2m+1}. \quad (49)$$

The simplest function f is obtained for $m = 0$ and corresponds to a constant function of value λ_0 . In this case, Eq. (46) reduces to

$$NB_\phi = \lambda_0 (e+p)\Phi^2 N^2 r^2 \sin^2 \theta, \quad (50)$$

and thus

$$B_\phi = \lambda_0 (e+p)\Phi^2 N r^2 \sin^2 \theta, \quad (51)$$

supplemented by Eq. (49), which yields the simplified expression

$$\tilde{M} = \frac{\lambda_0^2}{4\pi} (e+p)\Phi^2 N^2 r^2 \sin^2 \theta. \quad (52)$$

For all models computed in this study, the magnetic-field component B_ϕ is given by Eq. (51) and the magnetic potential \tilde{M} by Eq. (52). Because \tilde{M} vanishes on the axis of symmetry, $\tilde{M}_c = 0$, and the integral of Eq. (41) reads

$$H + \nu - \ln \Gamma + \tilde{M} = H_c + \nu_c, \quad (53)$$

where H_c and ν_c are the central values of H and ν respectively. Note that a general prescription for the determination of the magnetic field B_ϕ and of the magnetic potential \tilde{M} can be found in Kiuchi & Yoshida (2008) and Gourgoulhon et al. (2011).

3.5 Perfect-conductor relation

According to Ohm's law and assuming an infinite conductivity for the neutron-star matter, the electric field \mathbf{E}' as measured by the fluid comoving observer \mathcal{O}_1 has to vanish, namely

$$E'_\alpha = F_{\alpha\beta} u^\beta = (0, 0, 0, 0). \quad (54)$$

In the case of a purely poloidal magnetic field (Bocquet et al. 1995), the perfect-conductor relation Eq. (54) is nontrivial as it establishes a dependence between A_r and A_θ and forces a dependence of the angular velocity on A_ϕ , i.e. $\Omega = \Omega(A_\phi)$. In the case of a purely toroidal magnetic field, on the other hand, the perfect-conductor condition is trivially satisfied and no condition is set on the rotation law, so that differentially-rotating models can be built as in the unmagnetised case.

It is thus possible to consider differentially rotating configurations following the procedure for the unmagnetised case. The magnetic field \mathbf{B}' as measured by the fluid comoving observer \mathcal{O}_1 now becomes

$$\begin{aligned} B'_\alpha &= -\frac{1}{2} \eta_{\alpha\beta\gamma\delta} F^{\gamma\delta} u^\beta \\ &= \frac{\Gamma \Phi \sin \theta}{\Psi^2} \left(\Omega \left[\frac{\partial A_\theta}{\partial r} - \frac{\partial A_r}{\partial \theta} \right], 0, 0, - \left[\frac{\partial A_r}{\partial \theta} - \frac{\partial A_\theta}{\partial r} \right] \right). \end{aligned} \quad (55)$$

Note that $B'_t + \Omega B'_\phi = 0$ and that $B'_\phi = \Gamma B_\phi$.

3.6 Equation of state

To solve the system of equations introduced in the previous Section, we need a prescription relating the energy density e and pressure p to the baryon number density n . The simplest of such relations is offered by the polytropic EOS, in which case the following identities hold

$$e(n) = m_b n + \kappa \frac{n^\gamma}{\gamma - 1}, \quad (56)$$

$$p(n) = \kappa n^\gamma, \quad (57)$$

where κ is the polytropic constant and γ the adiabatic index. Combining Eq. (40) and Eqs. (56), (57), the log-enthalpy H and n can be expressed as functions of each other, namely, as

$$H(n) = \ln \left(1 + \frac{\kappa}{m_b} \frac{\gamma}{\gamma - 1} n^{\gamma-1} \right), \quad (58)$$

$$n(H) = \left(\frac{\gamma - 1}{\gamma} \frac{m_b}{\kappa} (e^H - 1) \right). \quad (59)$$

Hereafter, we will assume $\gamma = 2$ and refer to this EOS as to Pol2. In addition to the Pol2 EOS, we have considered a sample of

seven single-constituent one-parameter EOS treating the neutron-star matter as a perfect fluid and derived from very different models of the ground state of cold (zero temperature) dense matter in this work as they are provided by the LORENE library.

More specifically, we have considered the APR EOS (Akmal et al. 1998), the BBB2 EOS (Baldo et al. 1997), the BN1H1 EOS (Balberg & Gal 1997), the BPAL12 EOS (Bombaci 1995), the FPS EOS (Pandharipande & Ravenhall 1989), the Sly4 EOS (Douchin & Haensel 2001), and the GNH3 EOS (Glendenning 1985). All of these realistic EOSs are provided in tabulated form, which requires the interpolation of listed thermodynamical quantities n , e , and p between contiguous sampling points. Thermodynamical consistency of the interpolated values is ensured by an interpolation procedure based on Hermite polynomials introduced by Swesty (1996), which is crucial for the accuracy of the resulting numerical models (Salgado et al. 1994).

The properties of the spherical nonrotating and unmagnetised reference models with a gravitational mass of $M = 1.400 M_\odot$ can be found in Table 5. The softest EOS of this sample is the BPAL12 EOS, which yields the smallest circumferential radius of $R_{\text{circ}} = 10.06$ km, whereas the stiffest one is the GNH3 EOS, which yields the largest circumferential radius of $R_{\text{circ}} = 14.20$ km.

3.7 Global quantities

A number of global quantities which characterise the numerical models presented in this study can be computed and will be needed in the course of this investigation. These are: the gravitational mass

$$M \equiv \int N \Psi^2 \Phi \left(E + S + \frac{2}{N} N^\phi J_\phi \right) r^2 \sin \theta \, dr \, d\theta \, d\phi, \quad (60)$$

the total angular momentum

$$J \equiv \int \Psi^2 \Phi J_\phi r^2 \sin \theta \, dr \, d\theta \, d\phi, \quad (61)$$

the total magnetic energy

$$\mathcal{M} \equiv \int \Psi^2 \Phi \mathcal{E} r^2 \sin \theta \, dr \, d\theta \, d\phi, \quad (62)$$

the total kinetic energy

$$T \equiv \frac{1}{2} \Omega J, \quad (63)$$

and the gravitational binding energy

$$W \equiv M - T - M_p - \mathcal{M}, \quad (64)$$

where the total internal energy M_p is defined as

$$M_p \equiv \int \Psi^2 \Phi \Gamma e r^2 \sin \theta \, dr \, d\theta \, d\phi, \quad (65)$$

while the total baryon mass of the star is given by

$$M_b \equiv \int \Psi^2 \Phi \Gamma n r^2 \sin \theta \, dr \, d\theta \, d\phi. \quad (66)$$

Other important quantities that are more closely related to the deformation of the star are the circumferential radius R_{circ} , which is the equatorial radius as measured by the observer \mathcal{O}_0 and is related to the equatorial coordinate radius R according to

$$R_{\text{circ}} \equiv \Phi(R, \pi/2) R, \quad (67)$$

the surface deformation (or apparent oblateness)

$$\epsilon_s \equiv r_e/r_p - 1, \quad (68)$$

where r_e , r_p are the equatorial and polar coordinate radii, respectively, and the quadrupole distortion ϵ of the star (Bonazzola & Gourgoulhon 1996)

$$\epsilon \equiv -\frac{3}{2} \frac{\mathcal{J}_{zz}}{I}, \quad (69)$$

where \mathcal{J}_{zz} is the quadrupole moment measured in some asymptotically Cartesian mass-centred coordinate system (Thorne 1980), while the moment of inertia $I = I_{zz}$ is defined as $I \equiv J/\Omega$. We stress that no moment of inertia other than the latter can be defined in a meaningful way for axisymmetric rotating bodies and that the rotation must be rigid and about the axis of symmetry. Furthermore, we note that $-(3/2)\mathcal{J}_{zz}$ differs from the standard quadrupole moment Q and that in the case of QI coordinates, the latter can be read off from the asymptotic expansion of $\ln N$ according to

$$\ln N = -\frac{M}{r} + \frac{M^2}{12r^3} + \frac{Q}{r^3} P_2(\cos \theta) + \dots \quad (70)$$

Thorne's quadrupole moment \mathcal{J}_{zz} is the relevant quantity when the gravitational-wave emission from a distorted star has to be determined, and the corresponding values are extracted from the asymptotic expansion of certain components of the metric tensor g in QI coordinates following the procedure presented in Bonazzola & Gourgoulhon (1996).

4 NUMERICAL IMPLEMENTATION AND TESTS

4.1 Numerical scheme

The analytic scheme presented in Sect. 3 has been implemented by extending an existing multi-domain, surface-adaptive spectral method for unmagnetised relativistic stars presented in Bonazzola et al. (1998); Gourgoulhon et al. (1999) and part of the LORENE¹ C++ class library for numerical relativity. We refer to Bonazzola et al. (1998); Gourgoulhon et al. (1999) for a detailed description of the numerical method and of the tests carried out. The numerical solution is computed by iteration, starting from crude initial conditions of a parabolic log-enthalpy profile, no rotation, flat space and no magnetic field. Convergence is monitored by computing $\|H_n - H_{n-1}\|/\|H_{n-1}\|$ where $\|H_{n-1}\|$ is the sum of the absolute values of the log-enthalpy H over all collocation points at iteration step $n - 1$. A convergent solution is assumed to be found when the normalized log-enthalpy residual decreases below a prescribed threshold, which is usually chosen to be of the order of 10^{-8} or smaller. The computational domain is divided into a spherical nucleus containing the star and two shells covering the exterior, where the last one maps onto a finite interval the whole exterior space, from a certain radius R up to spatial infinity. The default number of collocation points used in our study has been $n_\theta = 17$ in the angular direction and $\mathbf{n}_R = (33, 33, 17)$ in the radial direction, where the different numbers refer to the nucleus and the two shells, respectively. However, depending on the circumstances, the numerical resolution has been increased when necessary, i.e. up to $n_\theta = 129$ and $\mathbf{n}_R = (257, 257, 129)$ in the case of huge models with a matter distribution strongly deviating from a spherical one [cf. Table 2 and Fig. 6].

| | γ | 2 | 5/3 | 3/2 | 4/3 | 9/7 |
|------------------------|------------------|----------|----------|----------|----------|----------|
| Sood and Trehan (1972) | (ϵ/h) | -0.21377 | -0.14284 | -0.09292 | -0.03374 | -0.01724 |
| This work | (ϵ_s/h) | -0.21376 | -0.14218 | -0.09292 | -0.03374 | -0.01724 |

Table 1. Comparison of results for the normalized oblateness ϵ_s/h computed in the Newtonian limit for various polytropic EOS with results from Sood & Trehan (1972) (values for ϵ/h from table I where $\epsilon = (r_e - r_p)/r_0$ and r_0 is the radius of the unperturbed model). The perturbation parameter $h = \lambda_0^2/4\pi^2$ is a measure of the strength of the magnetic field.

4.2 Comparison with Newtonian results

The results of the numerical scheme in the Newtonian limit have been compared with those of an earlier investigation in the Newtonian regime. Sood & Trehan (1972) have in fact computed linear perturbations of polytropic stars induced by a toroidal magnetic field corresponding to the Newtonian limit of Eq. (51), namely

$$\frac{B_\phi}{r \sin \theta} = \lambda_0 \rho r \sin \theta, \quad (71)$$

where ρ denotes the Newtonian mass density. In Table 1, we show normalized values of the resulting oblateness for different adiabatic exponents produced with the present code and the corresponding results from Sood & Trehan (1972). We note that Sood & Trehan (1972) measured the deformation as $\epsilon_s = (r_e - r_p)/r_0$ where r_0 is the radius of the unperturbed model. Values computed according to this definition coincide with $\epsilon_s = r_e/r_p - 1$ within the rounding error of tabulated values. Clearly, for the perturbation parameter $h = \lambda_0^2/4\pi^2$, the respective values of ϵ_s/h agree to within 10^{-5} , except for $\gamma = 5/3$, for which the difference is about 10^{-3} . However, for $\gamma = 5/3$, certain functions intervening in the solution of the perturbed Lane-Emden equation become singular at the surface of the star (Das & Tandon 1977), suggesting a larger numerical error for the $\gamma = 5/3$ case as computed by Sood & Trehan (1972).

4.3 Virial identities

In order to monitor the global error of the numerical models computed with the new code we have calculated the two general-relativistic virial identities GRV2 (Bonazzola 1973; Bonazzola & Gourgoulhon 1994) and GRV3 (Gourgoulhon & Bonazzola 1994). We recall that these identities have to be fulfilled by any solution to the Einstein equations Eqs. (14)–(17) and are not enforced during the iterative procedure that leads to the solution. The GRV2 identity, in particular, has been shown to be directly related to the global error of a numerical solution (Bonazzola et al. 1993), while the GRV3 identity is an extension of the virial theorem of Newtonian physics to general relativity [see Nozawa et al. (1998) for details of the practical implementation]. For strongly-magnetised nonrotating models based on a polytropic EOS with $\gamma = 2$ and the moderate number of collocation points specified in Sect. 4.1, the violations to the identities GRV2 and GRV3 have been found to be the order of 10^{-6} or better. For the huge models listed in Table 2, corresponding values are of the order of 10^{-4} which required the number of collocation points to be multiplied by a factor eight compared to their default values. In the case of rapid rotation, on the other hand, the numerical grid is not perfectly adapted to the stellar surface, and the spectral approximation suffers from Gibbs phenomena, as reported in Bonazzola et al. (1993). However, the

corresponding values of the identities GRV2 and GRV3 are still of the order of 10^{-5} . For realistic EOS, values of GRV2 and GRV3 are of the order of 10^{-4} or better.

5 NONROTATING MAGNETISED MODELS

Nonrotating models of neutron stars with a toroidal magnetic field always generate *static* spacetimes for which the time Killing vector e_0 is hypersurface-orthogonal. Note that this assumption does not always hold in the case of a poloidal magnetic field because the additional presence of an electric field gives rise to an azimuthal Poynting vector [cf. Bonazzola et al. (1993)], which introduces a nonzero angular momentum even when the star does not rotate. As a consequence, the shift vector component N^ϕ does not vanish.

Although we are interested in the construction of rapidly rotating models (that we will present in Sect. 6), nonrotating configurations allow us to investigate the effects of the magnetic field without the influence of rotationally-induced effects. As a representative example, Fig. 2 shows isocontours of the magnetic-field strength and baryon number density for the nonrotating model PP-Po12 built with the Po12 EOS and for the maximum field strength (the physical properties of model PP-Po12 are listed in Table 4). The unmagnetised reference model with a circumferential radius of $R_{\text{circ}} = 12.00$ km is symbolised by a gray disc. In agreement with the simple structure function defined in Eq. (51), the toroidal magnetic field shown in the left panel vanishes on the axis of symmetry, reaches a maximum value of $B_{\text{max}} = 7.408 \times 10^{17}$ G in the equatorial plane deep inside the star, and decreases towards the surface of the star, where it vanishes, so that the magnetic field is fully contained inside the star. The forces exerted by the magnetic field can be visualised through the magnetic potential \tilde{M} , which shows a distribution similar to that of the magnetic-field strength and that, for this reason, we do not report here. It should be noted that the magnetic potential \tilde{M} is *repulsive*, since it is positive everywhere by construction. This is to be contrasted with the magnetic potential associated with the purely poloidal magnetic field adopted in Bocquet et al. (1995), that was instead *attractive*. As a result, the corresponding forces are the opposite, despite the isocontours appear to be very similar. Note also that in the present case of a purely toroidal magnetic field defined according to Eq. (51), the isocontours of \tilde{M} coincide with the flow lines of the electric current \mathbf{j} , which are nested loops in the meridional plane. Finally, we note that \tilde{M} vanishes at the surface of the star, implying that the latter coincides with an isosurface of the gravitational potential ν , as required by Eq. (53) when $\ln \Gamma = 0$ and $\tilde{M} = 0$.

The forces that can be derived from \tilde{M} vanish on the axis of symmetry and reach their maximum in the equatorial plane. Between the centre of the star and the maximum of \tilde{M} , they are directed inwards, inducing an approximately cylindrical compression of the central region of the star, which responds by a prolate deformation visible in the right panel of Fig. 2. In the outer layers of

¹ <http://www.lorene.obspm.fr>

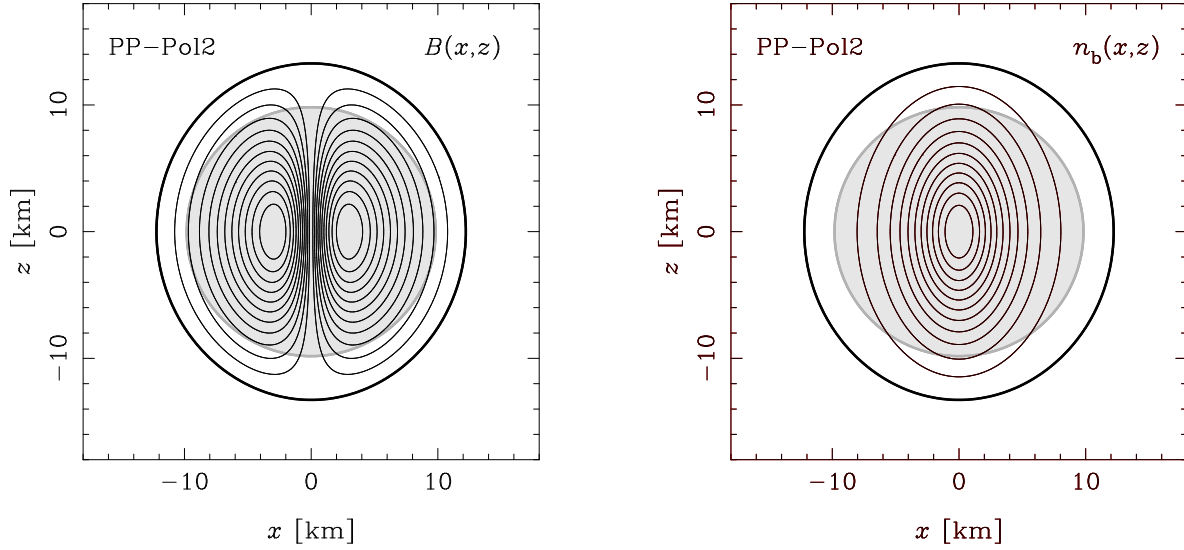


Figure 2. Isocontours of magnetic-field strength (left panel) and baryon number density (right panel) in the (x, z) plane of model PP-Pol2 of a nonrotating star with a gravitational mass of $M = 1.400 M_{\odot}$ and a circumferential radius of $R_{\text{circ}} = 12.00$ km in the unmagnetised case built with a polytropic EOS with $\gamma = 2$ for a maximum average magnetic-field strength of $\langle B^2 \rangle^{1/2} = 2.917 \times 10^{17}$ G. The gray disc indicates the dimensions of the unmagnetised reference model. Physical properties of model PP-Pol2 are listed in Table 4.

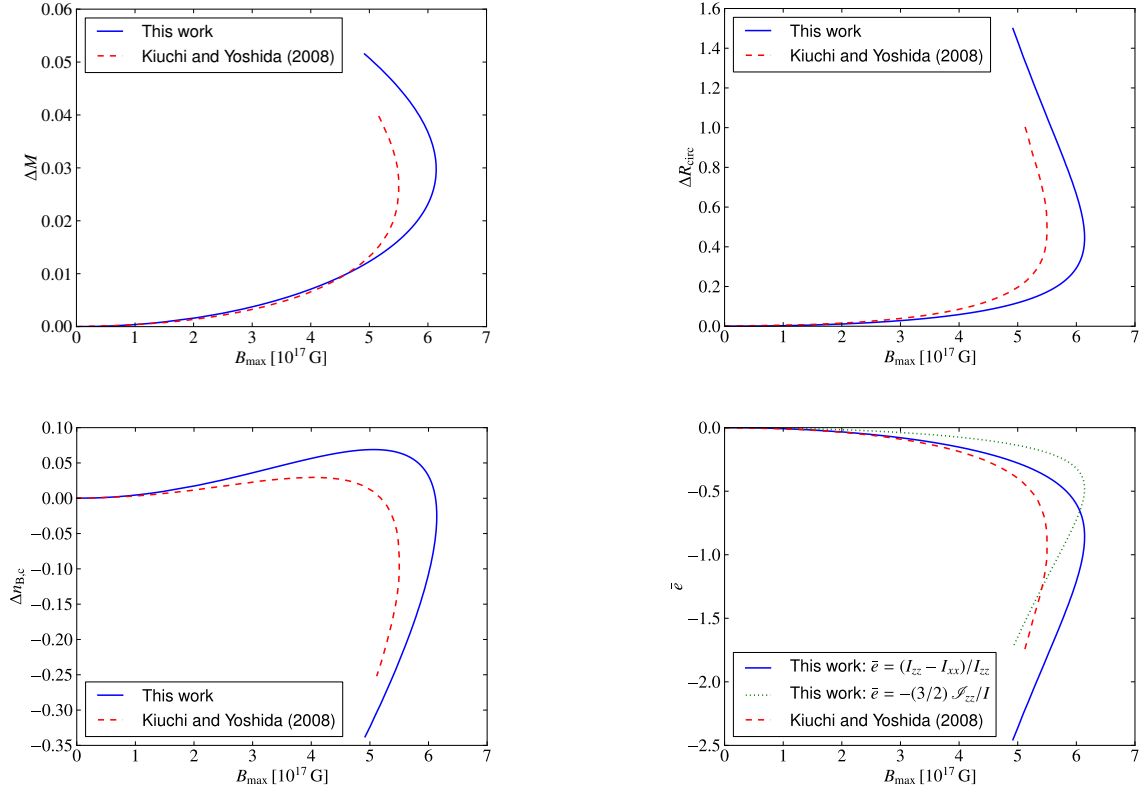


Figure 3. Comparison of the gravitational mass M , circumferential radius R_{circ} , central baryon number density $n_{b,c}$, and mean deformation $\bar{\epsilon}$ along with the maximum magnetic-field strength B_{max} attained inside the star as a function of the magnetisation parameter λ_0 for a Pol2 EOS model with a baryon mass of $M_b = 1.680 M_{\odot}$ and a circumferential radius of $R_{\text{circ}} = 14.30$ km in the unmagnetised case with results of Kiuchi & Yoshida (2008). The relative variation of some quantity χ is defined as $\Delta\chi(B_{\text{max}}, M_b) \equiv (\chi(B_{\text{max}}, M_b) - \chi(0, M_b)) / \chi(0, M_b)$.

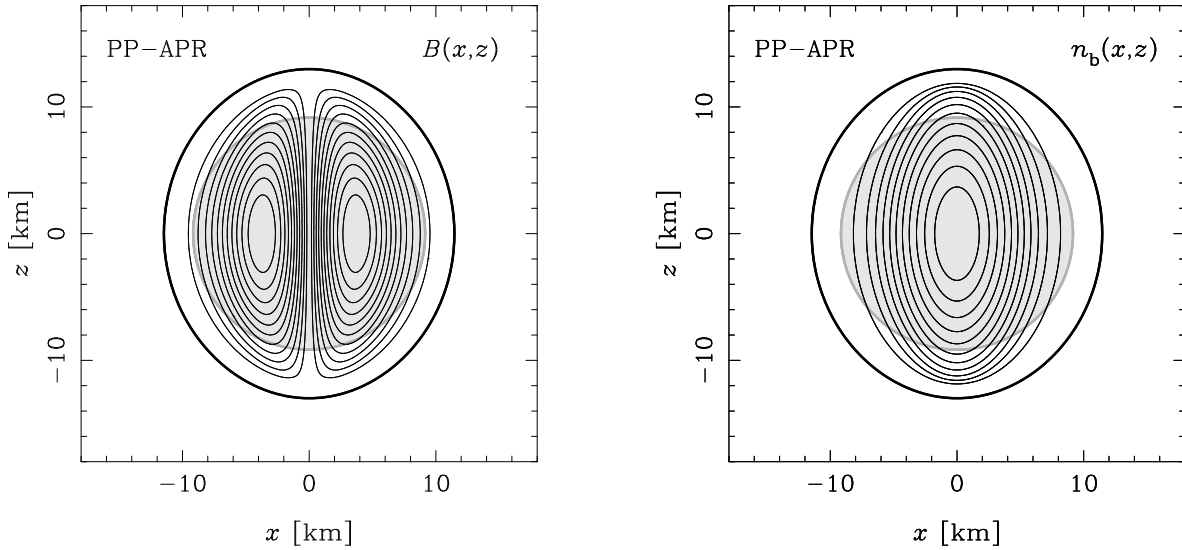


Figure 4. Isocontours of magnetic-field strength (left panel) and baryon number density (right panel) in the (x, z) plane of model PP-APR of a nonrotating star with a gravitational mass of $M = 1.400 M_{\odot}$ and a circumferential radius of $R_{\text{circ}} = 11.34$ km in the unmagnetised case built with the APR EOS for a maximum average magnetic-field strength of $\langle B^2 \rangle^{1/2} = 3.597 \times 10^{17}$ G. The gray disc indicates the dimensions of the unmagnetised reference model. The physical properties of model PP-APR are listed in Table 4.

the star, on the other hand, the magnetic forces are directed radially outward, pushing them away from the centre, which results in a growth of the dimensions of the star whose circumferential radius has increased now to a value of $R_{\text{circ}} = 14.34$ km.

Both the apparent shape and the matter distribution are prolate, corresponding to negative values of the surface deformation and of the quadrupole distortion, namely $\epsilon_s = -0.0806$ and $\epsilon = -0.1986$, respectively. The value of ϵ_s is significantly smaller than that of ϵ , and this due to the fact that terms of higher order in the multipole expansion of the gravitational potential ν fall off rapidly while, at the same time, the surface of the star must coincide with an isosurface of ν . This interpretation is supported by the fact that this difference is significantly smaller for small perturbations around this model, as confirmed by comparing values of respective distortion coefficients b_B and c_B reported in Sect. 7.

The strength of the magnetic field is controlled by the magnetisation parameter λ_0 [cf. Eq. (52)], and the physical quantities associated with our models can be parametrized accordingly, in particular the maximum magnetic-field strength B_{max} . In Fig. 3, we compare our results with those reported in fig. 6 of Kiuchi & Yoshida (2008)², considering in particular the variation of the gravitational mass M , of the circumferential radius R_{circ} , of the central baryon number density $n_{b,c}$, and of the mean deformation \bar{e} . The comparison is made as a function of the maximum magnetic-field strength B_{max} and for a nonrotating reference model built with the Pol2 EOS and having a baryon mass of $M_b = 1.680 M_{\odot}$ and a circumferential radius of $R_{\text{circ}} = 14.30$ km in the unmagnetised case. For each of these quantities χ , we define the difference as $\Delta\chi(B_{\text{max}}, M_b) \equiv [\chi(B_{\text{max}}, M_b) - \chi(0, M_b)]/\chi(0, M_b)$. We note that in Kiuchi & Yoshida (2008) the mean deformation is defined as $\bar{e} \equiv (I_{zz} - I_{xx})/I_{zz}$, where I_{xx}, I_{zz} are the momenta of inertia relative to the corresponding axes [cf. Eq. (3.12) of Kiuchi & Yoshida

(2008)]; this measure is similar but different from our measure of the quadrupole distortion ϵ^3 .

The most prominent feature of this comparison is that B_{max} is not a monotonic function of λ_0 , thus being responsible for the presence of a turning point located at a magnetic-field strength of $B_{\text{max}} = 6.141 \times 10^{17}$ G. While our results (blue solid lines) agree qualitatively with those of Kiuchi & Yoshida (2008) (red dashed lines), we find significant quantitative differences for all of the quantities considered, the largest one being an increase in $n_{b,c}$ of 7% against the smaller 3% increase found by Kiuchi & Yoshida (2008). Another important difference is in the values of the maximum magnetic-field strength, which is $B_{\text{max}} = 6.141 \times 10^{17}$ G for us and $B_{\text{max}} = 5.503 \times 10^{17}$ G for Kiuchi & Yoshida (2008). The differences between the two calculations are smaller when comparing the mean deformations \bar{e} , but only for moderate values of B_{max} . Furthermore, the measure of \bar{e} is considerably different from the quadrupole deformation ϵ (green dotted line), suggesting that the definition of \bar{e} is not suitable for estimating the gravitational-wave emission of a distorted star because it overestimates corresponding values by about a factor of two for this reference model. Similar differences in the values of \bar{e} and ϵ have been found also for the unmagnetised model with a baryon mass of $M_b = 1.780 M_{\odot}$ rotating at $\Omega = 3.230 \times 10^3 \text{ s}^{-1}$ from table IV of Kiuchi & Yoshida (2008); in this case, the respective values of the mean deformation of $\bar{e} = 0.07764$ and $\bar{e} = 0.07462$, differ by about 4%, the quadrupole distortion for the same model is $\epsilon = 0.03870$ which is again only half of the value of \bar{e} .

In addition to the polytropic Pol2 EOS, we have computed nonrotating models for the sample of realistic EOSs discussed in Sect. 3.6 and for reference models having a gravitational mass of $M = 1.400 M_{\odot}$ in the unmagnetised case (basic physical properties of the unmagnetised reference models are collected in Table 5). Be-

² The data from fig. 6 of Kiuchi & Yoshida (2008) has been read off with the utility g3DATA, see <https://github.com/pn2200/g3data>.

³ More specifically, the definition of \bar{e} is valid only in a Newtonian framework, where $(I_{zz} - I_{xx})/I_{zz} = (I - I_{xx})/I = Q_{\text{Newt}}/I$, and Q_{Newt} is the Newtonian quadrupole moment.

cause we cannot show equilibrium models for all of these models, we have decided to use as alternative reference EOS the APR one and to complement model PP-Po12 at the maximum field-strength limit, with the corresponding model PP-APR, which nicely illustrates the impact of a prototypical realistic EOS on the resulting equilibrium model.

Figure 4 shows isocontours of magnetic-field strength and baryon number density for model PP-APR at the maximum field-strength limit, whose physical properties are collected in Table 4 (again, the dimensions of the unmagnetised reference model with a circumferential radius of $R_{\text{circ}} = 11.34$ km are indicated by a grey disc). The maximum magnetic-field strength attains a value of $B_{\text{max}} = 8.046 \times 10^{17}$ G in the equatorial plane. Because the APR EOS is stiffer than the Pol2 EOS, the matter distribution appears less condensed and the peaks of the magnetic field have moved slightly outwards. Moreover, both the surface deformation $\epsilon_s = -0.1176$ and the quadrupole distortion $\epsilon_s = -0.3045$ are larger than the corresponding values of model PP-Po12 by $\sim 50\%$. In contrast with model PP-Po12, a substantial fraction of the stellar interior below the surface appears to be field-free. This is easy to understand: according to Eq. (51), in fact, the amplitude of the toroidal magnetic field is proportional to $(e + p)$, so that the presence of a low-density crust as in the APR EOS suppresses the presence of a toroidal magnetic field in the outer layers of the star. The contour of the unmagnetised reference model not only emphasises the significant prolate deformation of the maximum field strength model, but also the important increase in the dimensions of the star.

Overall, the nonrotating models built with realistic EOSs show a behaviour which is qualitatively similar to that of the polytropic Pol2 EOS as shown in Table 3 and, for increasing magnetisation, all realistic EOS exhibit a maximum value of the magnetic-field strength $\langle B^2 \rangle^{1/2}$, beyond which it then decreases. The smallest value is obtained for the GNH3 EOS, with $\langle B \rangle \equiv \langle B^2 \rangle^{1/2} = 2.161 \times 10^{17}$ G; the largest one is instead obtained for the BPAL12 EOS, with $\langle B^2 \rangle^{1/2} = 4.790 \times 10^{17}$ G. Relevant data for all maximum field strength models is collected in Table 3 and reveals that the values of the maximum magnetic-field strength decrease with increasing circumferential radii R_{circ} , and which itself is a telltale of the stiffness of the EOS. As a result, the soft BPAL12 EOS with a circumferential radius of only $R_{\text{circ}} = 11.83$ km yields the model with the highest maximum magnetic-field strength, while the stiff GNH3 EOS the model with the lowest one.

We note that in Fig. 3, we have employed the peak magnetic-field strength B_{max} and not the average magnetic-field strength $\langle B^2 \rangle^{1/2}$, which reaches its turning point already at a lower magnetisation level. For this reason, all models based on a realistic EOS are located in a region where $\Delta n_{b,c} > 0$, as can be seen by a comparison with the related values of the unmagnetised models compiled in Table 5. The maximum values of the peak magnetic-field strength B_{max} are sensibly larger than those of the average magnetic-field strength $\langle B^2 \rangle^{1/2}$, attaining their maximum value for the model built with the FPS EOS with $B_{\text{max}} = 1.210 \times 10^{18}$ G.

The slight increase of the gravitational mass is the result of different contributions, which can be illustrated by the example of the PP-Po12 model. More specifically, the increase by $0.02682 M_{\odot}$ in the gravitational mass of the maximum field-strength model with respect to the unmagnetised model. This increase is the sum of a positive contribution of $0.03036 M_{\odot}$ due to the total magnetic energy, of a negative contribution of $-0.02160 M_{\odot}$ due to the internal energy lost because of the increased volume, and of a positive contribution of $0.01806 M_{\odot}$ by which the magnetised model is less gravitationally bound than its unmagnetised counterpart. Further-

more, all maximum field-strength models exhibit smaller momenta of inertia than in the unmagnetised case because of the lateral compression of the stellar core. Finally, we note that after reaching a minimum value, the momenta of inertia increase continuously with the magnetisation, as the growth of the dimensions of the star becomes significant.

The values of the surface deformation ϵ_s and of the quadrupole distortion ϵ obtained for our sample of maximum field-strength models also show a noticeable dependence on the stiffness of the EOS. In particular, the value of ϵ decreases (its absolute value increasing) with the increase of the circumferential radius R_{circ} . The Pol2 EOS model appears somehow at variance with this trend, but we believe this is caused by our choice of a comparatively large circumferential radius of $R_{\text{circ}} = 12.00$ km in the unmagnetised case, and which does not reflect the rather soft character of this EOS. Lower and upper bounds for the quadrupole distortion are set by the two extremal EOS of our sample: the model built with the soft EOS BPAL12 with a radius of less than 12.00 km exhibits the smallest quadrupole distortion despite of the largest ratio of magnetic energy to binding energy, whereas the large GNH3 model with a radius of 17.06 km shows the largest quadrupole distortion for the lowest ratio of magnetic energy to binding energy of the whole sample.

Much of what discussed so far is summarised in Fig. 5, where we present the dependence of the surface deformation ϵ_s and of the quadrupole distortion ϵ on the average magnetic-field strength $\langle B^2 \rangle^{1/2}$, for the representative Pol2 EOS and the APR EOSs. Note that up to $\langle B^2 \rangle^{1/2} \simeq 2.0 \times 10^{17}$ G, the behaviour of both distortions is essentially the same for the two EOSs and an almost perfectly linear function⁴ of $\langle B^2 \rangle$. This is not particularly surprising and indeed earlier Newtonian studies (Wentzel 1960; Ostriker & Gunn 1969) have suggested to parametrize the quadrupolar distortion ϵ_{Newt} induced in a self-gravitating incompressible fluid by a toroidal magnetic field as a simple function of the ratio of the magnetic energy to the binding energy, and hence as a function which is quadratic in the magnetic-field strength. Figure 5 suggests therefore that this behaviour is preserved also in general relativity and up to very large magnetic fields, thus offering the possibility of expressing the magnetic-induced deformation in terms of a simple algebraic expression with coefficients which will correct the previously known Newtonian ones. A more detailed discussion of this point is presented in Sect. 7 and in Appendix A.

We conclude this Section by commenting on a novel and particularly interesting result of our analysis of nonrotating configurations, namely, that no physical or numerical limit was found for the magnetisation level. More specifically, after suitably increasing the number of collocation points according to the desired level of accuracy, we were able to find solutions with very large values of the surface and quadrupolar deformations. As an example, we could obtain convergent solutions of the nonrotating reference model of Kiuchi & Yoshida (2008) with a baryon mass of $M_b = 1.680 M_{\odot}$ and a circumferential radius of $R_{\text{circ}} = 14.30$ km in the unmagnetised case, now strongly magnetised and attaining a circumferential radius of $R_{\text{circ}} = 101.5$ km and a related value of $\Delta R_{\text{circ}} = 6.098$. While the average magnetic-field strength $\langle B^2 \rangle^{1/2} = 0.1461 \times 10^{17}$ G is about an order of magnitude smaller than the maximum value of $\langle B^2 \rangle^{1/2} = 2.241 \times 10^{17}$ G reached at a circumferential radius of $R_{\text{circ}} = 17.09$ km, the ratio of magnetic energy to binding energy is

⁴ This is not straightforward to deduce from our Fig. 5, which reports ϵ_s and ϵ as a function of $\langle B \rangle$. However, it is very apparent when plotting the distortions as a function $\langle B^2 \rangle$ (not reported here for compactness).

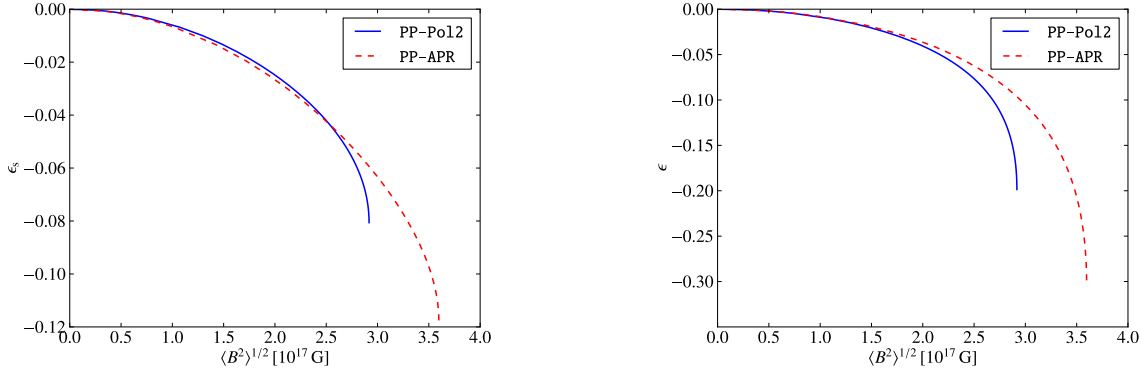


Figure 5. Surface deformation ϵ_s (left panel) and quadrupole distortion ϵ_b (right panel) for nonrotating models built with the Po12 EOS and the APR EOS as a function of the root mean square magnetic-field strength $\langle B^2 \rangle^{1/2}$ from the unmagnetised limit up to the maximum field strength models PP-Po12 and PP-APR, respectively. The physical properties of models PP-Po12 and PP-APR are listed in Table 4.

Table 2. Nonrotating neutron star models for large magnetisations of $\mathcal{M}/|W| \approx 0.5$. The gravitational mass is $M = 1.400 M_\odot$ for each EOS respectively in the unmagnetised and nonrotating case for which properties are listed in Table 5. B_{\max} is the maximum value of the magnetic field, $\langle B^2 \rangle^{1/2}$ the root mean square average of the magnetic-field strength determined over the volume of the star, $\mathcal{M}/|W|$ the absolute value of the ratio of total magnetic energy \mathcal{M} and potential energy W , $n_{b,c}$ the central baryon number density [0.1 fm^{-3}], M the gravitational mass, R_{circ} the circumferential radius, I the moment of inertia, ϵ_s the surface deformation, ϵ the quadrupole distortion, and GRV2/GRV3 the estimates of the global error of respective models based on the relativistic virial identities introduced in Sect. 4.3.

| Model | B_{\max} [10^{17} G] | $\langle B^2 \rangle^{1/2}$ [10^{17} G] | $n_{b,c}$ [0.1 fm^{-3}] | M [M_\odot] | R_{circ} [km] | I [10^{38} kg m^2] | $\mathcal{M}/ W $ | ϵ_s | ϵ | GRV2 | GRV3 |
|---------|---------------------------------------|--|--|----------------------|---------------------------|-------------------------------------|-------------------|--------------|------------|--------------------|--------------------|
| MM-Po12 | 2.514 | 0.1400 | 1.832 | 1.508 | 100.0 | 9.024 | 0.5006 | -0.2609 | -7.803 | 2×10^{-5} | 1×10^{-4} |
| MM-APR | 6.166 | 0.2313 | 4.219 | 1.544 | 90.26 | 4.909 | 0.5095 | -0.1248 | -4.810 | 8×10^{-6} | 1×10^{-4} |

much higher with values of $\mathcal{M}/|W| = 0.4868$ and $\mathcal{M}/|W| = 0.1308$ respectively. The surface deformation of this model reaches a value of $\epsilon_s = -0.2403$ and the quadrupole distortion an impressive value of $\epsilon = -6.946$. While clearly unrealistic for ordinary neutron stars, young proto-neutron stars may, in principle, attain these magnetizations and possibly these sizes (Villain et al. 2004); clearly, this represents a possibility that deserves a more careful investigation.

In order to illustrate the extreme effects of the toroidal magnetic field at high levels of magnetisation, we have computed model MM-Po12 of the Po12 EOS reference model with a gravitational mass of $M = 1.400 M_\odot$ and a circumferential radius of $R_{\text{circ}} = 12.00 \text{ km}$ in the nonrotating and unmagnetised case, now inflated to a circumferential radius of $R_{\text{circ}} = 100.0 \text{ km}$. Such an “extra-large” model is shown in Fig. 6, which, as the previous ones, reports the isocontours of magnetic-field strength (left panel) and baryon number density (right panel) for an average magnetic-field strength of $\langle B^2 \rangle^{1/2} = 0.1400 \times 10^{17} \text{ G}$. The physical properties of model MM-Po12 are listed in Table 2. In this case, therefore, the surface and quadrupolar deformations reach the extreme values of $\epsilon_s = -0.2609$ and of $\epsilon = -7.803$, respectively.

Although new and somewhat surprising, these results are not totally unexpected, and we note that already for a purely poloidal magnetic field, Cardall et al. (2001) doubted the existence of a mass-shedding limit in the nonrotating case. This leads to the conclusion that the non-convergence limit encountered by Kiuchi & Yoshida (2008) at $R_{\text{circ}} = 28.85 \text{ km}$ may be due to their numerical scheme. Furthermore, to confirm that the extreme distortions reported for model MM-Po12 are not a peculiarity of the Po12 EOS, we have found similar equilibria also for model MM-APR, built

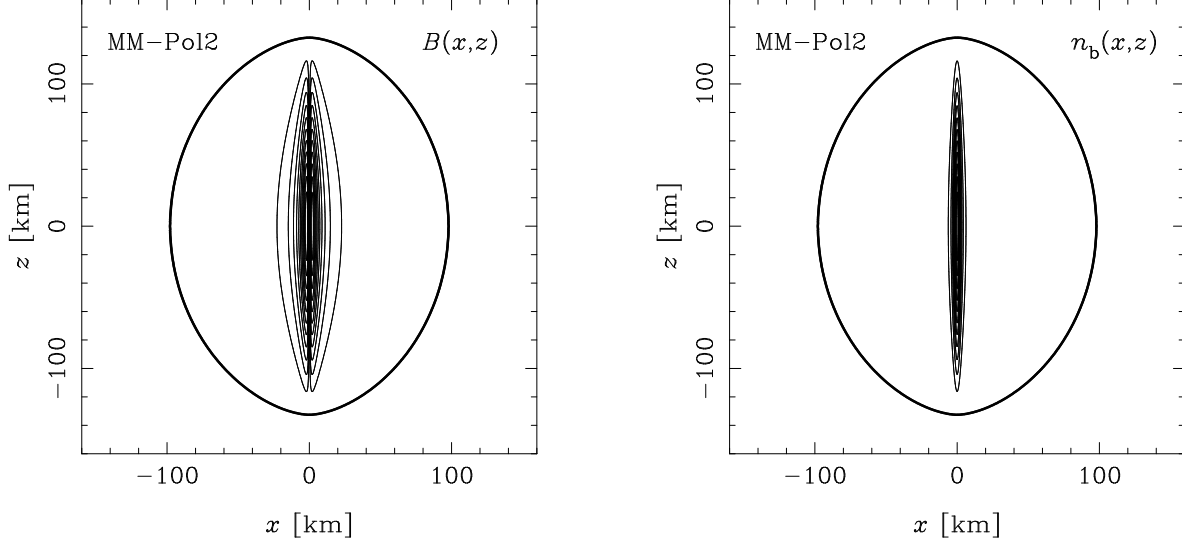
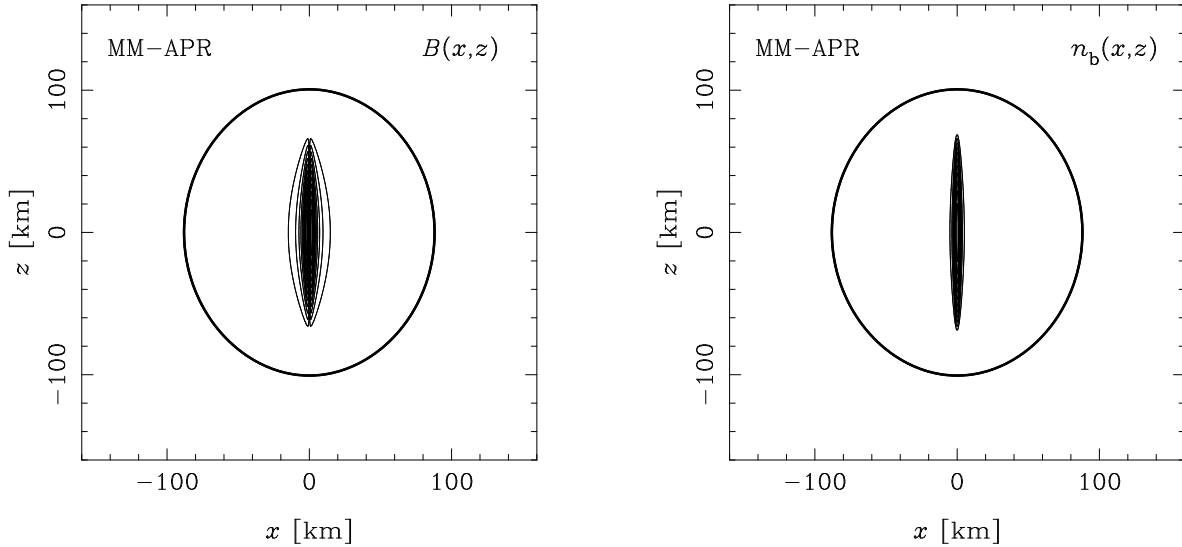
with the APR EOS with a gravitational mass of $M = 1.400 M_\odot$ and a circumferential radius of $R_{\text{circ}} = 11.34 \text{ km}$ in the unmagnetised case. This is shown in Fig. 7 and exhibits the same spindle-shaped matter distribution of the stellar core for a circumferential radius of $R_{\text{circ}} = 90.26 \text{ km}$ and an average magnetic-field strength of $\langle B^2 \rangle^{1/2} = 0.2313 \times 10^{17} \text{ G}$. The physical properties of model MM-APR are listed in Table 2, but we note here that the surface and quadrupolar deformations reach the extreme values of $\epsilon_s = -0.1248$ and of $\epsilon = -4.810$, respectively. These values are smaller than those of model MM-Po12 (despite the ratio of magnetic energy to binding energy is similar and $\mathcal{M}/|W| \approx 0.5$) but shows quite clearly that extremely large deformations are a feature of nonrotating models, independently of the EOS.

6 ROTATING MAGNETISED MODELS

Having investigated in the previous Section nonrotating models, we next turn to models that include rotation, which is well known to induce deformations of the stars that are the opposite of those discussed so far, namely, of introducing an oblateness generically both in the surface deformation and in the quadrupole distortion. In particular, we are concerned with determining the limits of the space of solutions both in terms of the magnetisation and of the rotation rate. To probe in detail such a space of solutions we consider two rotating models corresponding to maximum field-strength configurations of the Po12 EOS. The first of these reference models, which we refer to as P0-Po12, has a mean magnetic-field strength of $\langle B^2 \rangle^{1/2} = 2.324 \times 10^{17} \text{ G}$ and rotates at an angular velocity of $\Omega = 3.969 \times 10^3 \text{ s}^{-1}$, thus with a moderate ratio of kinetic en-

Table 3. The same as in Table 2 but for models computed with different EOSs at the maximum field-strength limit.

| EOS | B_{\max} [10^{17} G] | $\langle B^2 \rangle^{1/2}$ [10^{17} G] | $n_{b,c}$ [0.1 fm^{-3}] | M [M_{\odot}] | R_{circ} [km] | I [10^{38} kg m^2] | $\mathcal{M}/ W $ | ϵ_s | ϵ | GRV2 | GRV3 |
|--------|------------------------------|---|--|------------------------|---------------------------|-------------------------------------|-------------------|--------------|------------|---------------------|--------------------|
| Pol2 | 7.408 | 2.917 | 8.409 | 1.427 | 14.34 | 1.278 | 0.3186 | -0.0806 | -0.1986 | 7×10^{-11} | 3×10^{-9} |
| APR | 8.046 | 3.597 | 6.036 | 1.438 | 13.58 | 1.136 | 0.2922 | -0.1176 | -0.3045 | 5×10^{-7} | 4×10^{-7} |
| BBB2 | 8.475 | 3.781 | 7.132 | 1.439 | 13.31 | 1.093 | 0.3133 | -0.1138 | -0.2899 | 3×10^{-6} | 4×10^{-6} |
| BN1H1 | 6.414 | 2.830 | 7.174 | 1.432 | 15.14 | 1.319 | 0.2810 | -0.1086 | -0.3065 | 2×10^{-5} | 2×10^{-5} |
| BPAL12 | 12.10 | 4.790 | 13.91 | 1.438 | 11.83 | 0.897 | 0.4589 | -0.0782 | -0.1729 | 3×10^{-6} | 4×10^{-6} |
| FPS | 9.090 | 4.019 | 7.908 | 1.440 | 12.99 | 1.046 | 0.3308 | -0.1122 | -0.2809 | 1×10^{-5} | 2×10^{-5} |
| GNH3 | 5.090 | 2.161 | 4.182 | 1.427 | 17.06 | 1.605 | 0.1984 | -0.1083 | -0.3313 | 5×10^{-6} | 1×10^{-5} |
| SLy4 | 7.523 | 3.341 | 5.972 | 1.436 | 14.04 | 1.191 | 0.2848 | -0.1156 | -0.3076 | 6×10^{-6} | 3×10^{-6} |

**Figure 6.** Isocontours of magnetic-field strength (left panel) and baryon number density (right panel) in the (x, z) plane of model MM-Pol2 of a nonrotating star with a gravitational mass of $M = 1.400 M_{\odot}$ and a circumferential radius of $R_{\text{circ}} = 12.00 \text{ km}$ in the unmagnetised case built with the Pol2 EOS for an average magnetic-field strength of $\langle B^2 \rangle^{1/2} = 0.1400 \times 10^{17} \text{ G}$. The physical properties of model MM-Pol2 are listed in Table 2.**Figure 7.** Isocontours of magnetic-field strength (left panel) and baryon number density (right panel) in the (x, z) plane of model MM-APR of a nonrotating star with a gravitational mass of $M = 1.400 M_{\odot}$ and a circumferential radius of $R_{\text{circ}} = 11.34 \text{ km}$ in the unmagnetised case built with the APR EOS for an average magnetic-field strength of $\langle B^2 \rangle^{1/2} = 0.2313 \times 10^{17} \text{ G}$. The physical properties of model MM-APR are listed in Table 2.

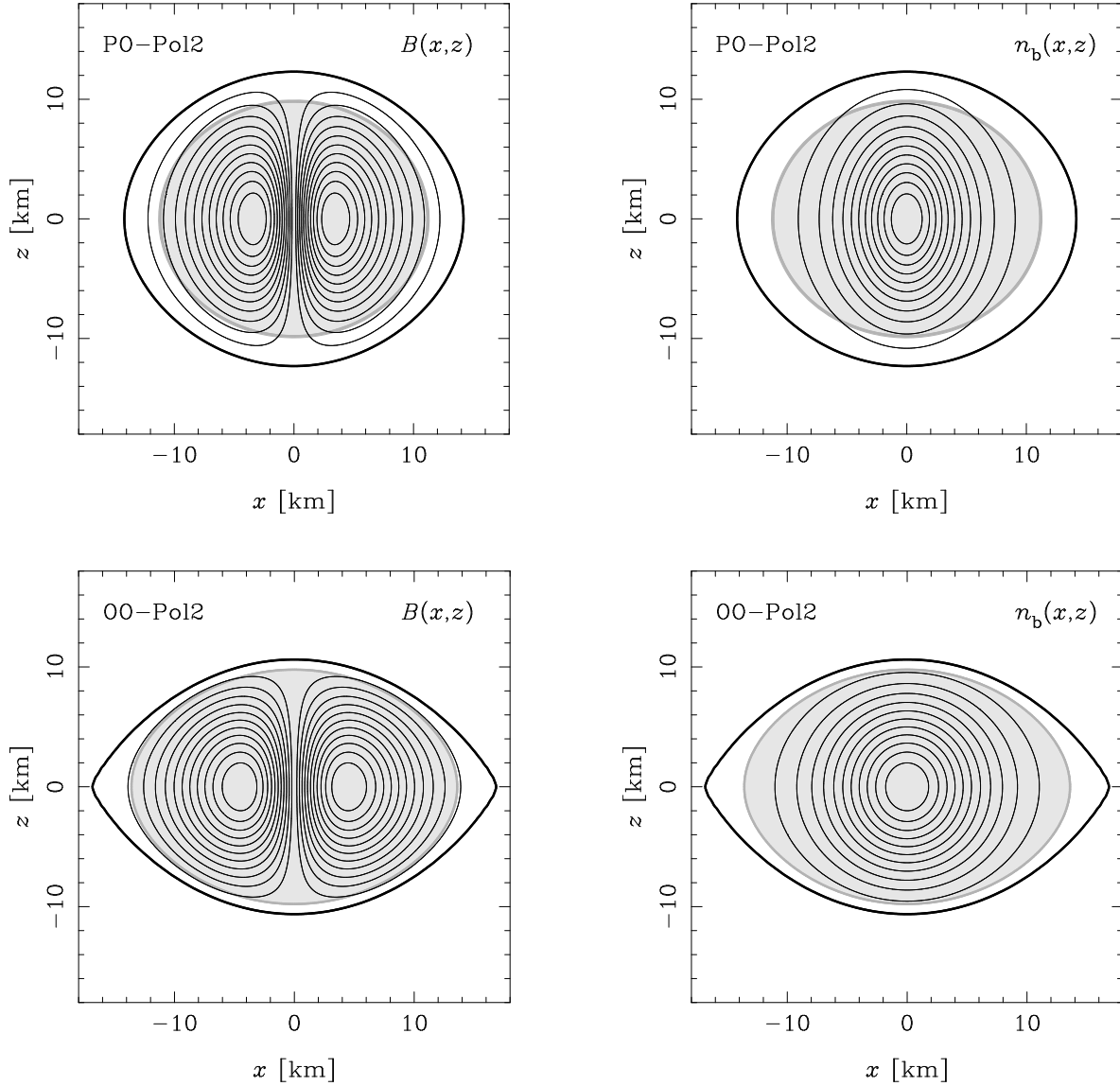


Figure 8. Isocontours of magnetic-field strength (left panel) and baryon number density (right panel) in the (x, z) plane of the PO-Pol2 and the OO-Pol2 models of a star built with a polytropic EOS with $\gamma = 2$ with a gravitational mass of $M = 1.400 M_\odot$ and a circumferential radius of $R_{\text{circ}} = 12.00$ km in the unmagnetised and nonrotating case which is now rotating at $\Omega = 3.969 \times 10^3 \text{ s}^{-1}$ (top) and $\Omega = 5.050 \times 10^3 \text{ s}^{-1}$ (bottom) respectively. The gray disc indicates the dimensions of the unmagnetised reference model. The physical properties of models PO-Pol2 and OO-Pol2 are listed in Table 4.

ergy to binding energy of $T/|W| = 0.03200$. The second model, that we refer to as OO-Pol2, has a mean magnetic-field strength of $\langle B^2 \rangle^{1/2} = 1.393 \times 10^{17} \text{ G}$ and rotates rapidly at an angular velocity of $\Omega = 5.050 \times 10^3 \text{ s}^{-1}$, with a ratio $T/|W| = 0.07136$ (see Table 4 for a complete list of the physical properties).

The magnetic-field strength and the baryon number density of both models are shown in Fig. 8, with the top row referring to PO-Pol2 and the bottom one to OO-Pol2. The denomination of these two models becomes apparent when considering the corresponding surface and quadrupole deformations. While in fact the qualitative properties of PO-Pol2 seem to resemble those of the nonrotating model PP-Pol2, the surface of this model is markedly flattened and indeed with a positive oblateness of $\epsilon_s = 0.1521$. The matter distribution inside the star, however, is still prolately deformed, as confirmed by a negative value of the quadrupole distortion, namely $\epsilon = -0.0684$. On the other hand, for model OO-Pol2

both the surface deformation and the quadrupole distortion are positive, i.e. $\epsilon_s = 0.5861$ and $\epsilon = 0.0856$, even though the isocontours of the baryon number density are still prolately toward the centre of the star. Interestingly, for model PO-Pol2, for which the magnetic field is still dominating, the ratio of the magnetic energy to the binding energy $\mathcal{M}/|W|$ exceeds that of the kinetic energy to the binding energy $T/|W|$, whereas for model OO-Pol2, the opposite is true. Hence, while this condition does not hold in all cases, we can take the inequality $\mathcal{M}/T \gtrsim 1$ as a first approximate criterion for the production of a negative quadrupole distortion. A more quantitative discussion on this will be presented in Sect. 7.

In our sampling of the space of parameter we have computed a total of more than 900 models of rotating and magnetised equilibrium configurations of the Pol2 EOS, which are *uniquely* labelled by the values of the angular velocity Ω and of the magnetisation parameter λ_0 . The latter extends up to a maximum obtained for a

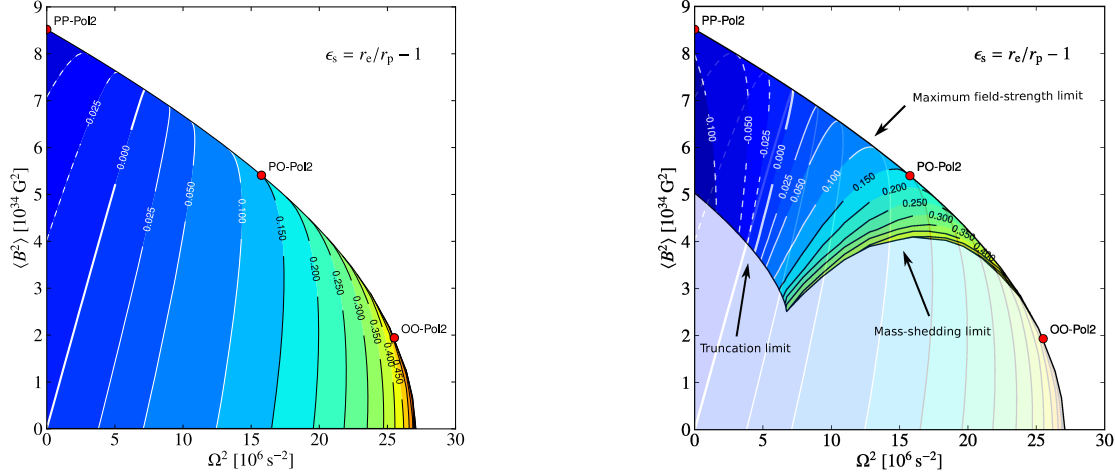


Figure 9. Isocontours of the surface deformation ϵ_s for the Pol2 EOS reference model with a gravitational mass of $M = 1.400 M_\odot$ and a circumferential radius of $R_{\text{circ}} = 12.00$ km in the unmagnetised and nonrotating case. The curved line which connects the nonrotating model with a maximum average magnetic-field strength of $\langle B^2 \rangle^{1/2} = 2.917 \times 10^{17}$ G with the unmagnetised model rotating at the mass-shedding limit of $\Omega = 5.205 \times 10^3 \text{ s}^{-1}$ separates the lower part of the solution space (left panel) where the mean magnetic-field strength increases as a function of the field strength parameter λ_0 from the upper part of the solution space (right panel) where the mean magnetic-field strength decreases as a function of the latter. In the right panel, we have also shown the lower sheet lying underneath.

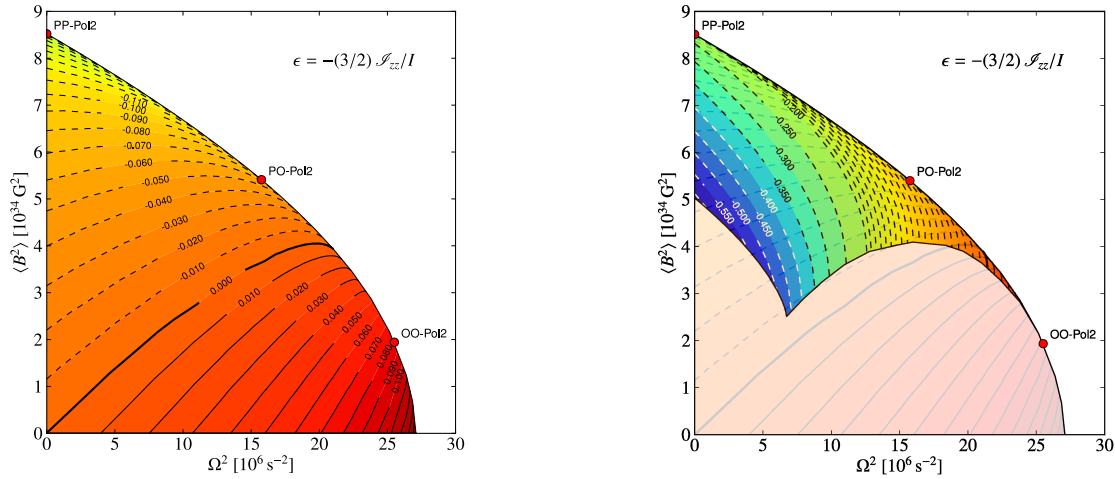


Figure 10. Isocontours of the quadrupole distortion ϵ for the Pol2 EOS reference model with a gravitational mass of $M = 1.400 M_\odot$ and a circumferential radius of $R_{\text{circ}} = 12.00$ km in the unmagnetised and nonrotating case. The curved line which connects the nonrotating model with a maximum average magnetic-field strength of $\langle B^2 \rangle^{1/2} = 2.917 \times 10^{17}$ G with the unmagnetised model rotating at the mass-shedding limit of $\Omega = 5.205 \times 10^3 \text{ s}^{-1}$ separates the lower part of the solution space (left panel) where the mean magnetic-field strength increases as a function of the field strength parameter λ_0 from the upper part of the solution space (right panel) where the mean magnetic-field strength decreases as a function of the latter. In the right panel we have also shown the lower sheet lying underneath.

nonrotating model with a radius of $R_{\text{circ}} = 19.45$ km and a ratio of magnetic energy to binding energy of $\mathcal{M}/|W| = 0.2448^5$. Overall, the space of physical solutions is delimited by four boundaries: (1) the nonrotating limit with $\Omega = 0$; (2) the unmagnetised limit with

⁵ Note that the “extra-large” models shown in Figs. 6 and 7 are located beyond the truncation limit and thus do not belong to what we consider the parameter space.

$B = 0$; (3) the (self-imposed) “truncation limit” with respect to the magnetisation parameter λ_0 ; (4) the mass-shedding limit, beyond which no rotating solution does exist.

We have already noted that for nonrotating models the mean magnetic-field strength $\langle B^2 \rangle^{1/2}$ is not a monotonic function of the magnetisation parameter λ_0 and that after attaining a maximum value of $\langle B^2 \rangle^{1/2} = 2.917 \times 10^{17}$ G, it decreases continuously as the magnetisation is increased. This behaviour has been found also for rotating models, thus implying a non-uniqueness for models in the

space $(\Omega^2, \langle B^2 \rangle)$. Such a degeneracy could be avoided by replacing the average magnetic-field strength with a quantity that grows monotonically with the magnetisation, e.g. the circumferential radius R_{circ} or the ratio of magnetic energy to binding energy $\mathcal{M}/|W|$. However, because of their fundamental astrophysical importance, we have chosen to report the results for the surface deformation ϵ_s and the quadrupole distortion ϵ in terms of the mean magnetic-field strength $\langle B^2 \rangle^{1/2}$ as the ordering quantity and of the angular velocity Ω . The presence of this degeneracy implies that when evaluated in the space of parameters $(\Omega^2, \langle B^2 \rangle)$, the distortions ϵ_s and ϵ will select a two-dimensional surface which can be split up along the turning points of maximum magnetic-field strength into a lower sheet, where $\langle B^2 \rangle^{1/2}$ increases as a function of the magnetisation parameter λ_0 , and an upper sheet, where the opposite happens. The left panel of Fig. 9, in particular, shows the surface deformation ϵ_s for the lower part of the solution space, while the right panel is its continuation beyond the turning point of $\langle B^2 \rangle^{1/2}$ and thus represents the upper sheet of the surface. Since nonrotating magnetised models always have a prolate shape, i.e. $\epsilon_s < 0$, while rotating unmagnetised models always have an oblate one, i.e. $\epsilon_s > 0$, it follows that rotating models between these limiting cases are divided into *prolate* ones and *oblate* ones by a neutral line $\epsilon_s = 0$. According to its definition in Eq. (68), the neutral line $\epsilon_s = 0$ does not require the stellar interior to be spherically symmetric and, indeed, when moving towards large values of the circumferential radius R_{circ} , models with comparable values of the equatorial and polar coordinate radii r_e, r_p (i.e. with $\epsilon_s \rightarrow 0$), show a progressively more pronounced “diamond shape” caused by an increasingly spindle-shaped matter distribution inside the star.

Unlike the magnetic potential, the centrifugal one is not confined to the star, and its influence increases moving away from the axis of rotation, reaching its minimum at the equator of the star. Note that $\tilde{M} = 0$ at the surface of the star, so that the latter is now an isosurface of the function $\nu - \ln \Gamma$ [cf. Eq. (53)]. From Fig. 9, we further infer that for any fixed angular velocity $\Omega \geq \Omega_0$, where $\Omega_0 = 2.594 \times 10^3 \text{ s}^{-1}$ is the maximum angular velocity at the magnetisation truncation limit, the mass-shedding limit is reached for some oblate shape and $\epsilon_s > 0$. Since the toroidal magnetic field is a source of additional pressure, augmenting the magnetisation not only increases the deformation of the surface and of the matter distribution, but it also causes an expansion, particularly of the circumferential radius R_{circ} . At a sufficient level of magnetisation, it will therefore be possible to reach the mass-shedding angular velocity, i.e. the rotation frequency such that the condition of geodesic motion at the equator is satisfied, and the star will develop the characteristic cusp at the equator. Because this angular frequency is smaller than the corresponding one for an unmagnetised model having the same rest-mass, the toroidal magnetic field indirectly sets a reduced limit of the spin frequency of these objects. In Fig. 9, this mass-shedding limit corresponds to the lower right boundary of the upper part of the solution space (see right panel) and along this limit, the Newtonian condition of geodesic motion, $\Omega^2 R_{\text{circ}}^3 = \text{const}$, is fulfilled. Note also that with the exception of the unmagnetised one, all mass-shedding models appear to belong to the upper sheet of the solution space. For models rotating at angular velocities up to that of model 00-Po12, i.e. $\Omega = 5.050 \times 10^3 \text{ s}^{-1}$, we have verified this proposition directly by determining the turning point of $\langle B^2 \rangle^{1/2}$; for even more rapidly rotating models for which the numerical determination of the maximum field-strength limit has not been conclusive, it is supported by extrapolating the boundary between lower and upper part of the solution space beyond model 00-Po12 towards the unmagnetised mass-shedding limit.

Using a small set of additional rotating models computed beyond the magnetisation truncation limit, we have started to explore the behaviour of the equilibrium models in these rather extreme conditions. Overall, we have found that the angular velocity of mass-shedding models decreases progressively, while the boundary associated with the mass-shedding limit and the neutral line $\epsilon_s = 0$ converge to the point $(\Omega^2, \langle B^2 \rangle) = (0, 0)$. These results suggest therefore that the solution at $(\Omega^2, \langle B^2 \rangle) = (0, 0)$ in the upper sheet of the space of solutions corresponds to the limit of a nonrotating model of infinite radius and vanishing mean magnetic-field strength. This fascinating suggestion clearly requires a more extensive analysis to be confirmed; we postpone this to a subsequent work.

Figure 9 also reveals that unlike in the unmagnetised rotating case with the same angular velocity Ω , all magnetised mass-shedding configurations behave qualitatively identically when the magnetisation is altered, namely: lowering their magnetisation moves them away from the mass-shedding limit. Accordingly, rotation becomes sub-critical, and the characteristic cusp at the equator disappears, which is accompanied by a decrease of the surface deformation. Slowly-rotating models pass through different stages as the magnetisation is lowered from the mass-shedding limit to the given angular velocity Ω down to the limit of vanishing magnetisation. More specifically, we find that: (i) below the mass-shedding limit, ϵ_s remains positive, but decreases continuously until the neutral line $\epsilon_s = 0$ is crossed for the first time; (ii) models then become increasingly prolate because the toroidal magnetic field becomes the principal source of deformation until they reach some negative minimum value of ϵ_s ; (iii) as the magnetisation is further decreased, ϵ_s increases progressively, and models eventually become oblate again when they cross the neutral line $\epsilon_s = 0$ for a second time, and rotation prevails over a decreasing toroidal magnetic field. For models rotating at moderate angular velocities of $3 \times 10^3 \text{ s}^{-1} \lesssim \Omega \lesssim 5 \times 10^3 \text{ s}^{-1}$, the behaviour is similar to that of slowly rotating ones, except that ϵ_s remains positive, so that the models always exhibit an oblate shape regardless of the level of magnetisation. Finally, rapidly rotating models with $\Omega \gtrsim 5 \times 10^3 \text{ s}^{-1}$ remain close to the magnetised mass-shedding limit regardless of the magnetisation level.

Generally speaking, for any fixed angular velocity Ω , the line $\Omega = \text{const}$ is tangential to exactly one level curve of ϵ_s . The touching point determines the magnetisation level for which the surface deformation attains its minimum. For decreasing angular velocity, these minima move to higher magnetisations and smaller values of ϵ_s . The angular velocity Ω' for which the maximum magnetic-field strength model exhibits $\epsilon_s = 0$ separates rotating models into two groups: (1) models rotating at $\Omega > \Omega'$ are always oblate, and the model of minimum (positive) surface deformation is located in the lower part of the solution space; (2) models rotating at $\Omega < \Omega'$ include a prolate model of minimum (negative) surface deformation which is located in the upper part of the solution space.

Figure 10 provides an equivalent representation of the data shown in Fig. 9 but this time in terms of the quadrupole distortion ϵ . Also in this case, the space of the numerical solutions is split into an upper sheet and a lower one, where the distinction is the same one as made for the surface distortion ϵ_s . For all models, ϵ increases monotonically as a function of the magnetisation, and the neutral line $\epsilon = 0$ extends from the nonrotating and unmagnetised reference model, up to a strongly-magnetised mass-shedding model with $\langle B^2 \rangle^{1/2} \approx 2 \times 10^{17} \text{ G}$ rotating at an angular velocity of $\Omega \approx 4.5 \times 10^3 \text{ s}^{-1}$, and with $T/|W| \approx 0.06$. Thus, even rapidly rotating models can exhibit a prolate matter distribution provided

Table 4. Neutron star models at the maximum field-strength limit. The gravitational mass is $M = 1.400 M_\odot$ for each EOS respectively in the unmagnetised and nonrotating case for which properties are listed in Table 5. B_{\max} is the maximum value of the magnetic-field strength, $\langle B^2 \rangle^{1/2}$ the root mean square value of the magnetic-field strength determined over the volume of the star, $\mathcal{M}/|W|$ the absolute value of the ratio of total magnetic energy \mathcal{M} and potential energy W , $n_{b,c}$ the central baryon number density [0.1 fm^{-3}], M the gravitational mass, R_{circ} the circumferential radius, I the moment of inertia, ϵ_s the surface deformation, ϵ_B the magnetic quadrupole distortion, and GRV2/GRV3 the estimates of the global error of respective models based on the relativistic virial identities introduced in Sect. 4.3.

| Model | B_{\max} [10^{17} G] | $\langle B^2 \rangle^{1/2}$ [10^{17} G] | $n_{b,c}$ [0.1 fm^{-3}] | M [M_\odot] | R_{circ} [km] | I [10^{38} kg m^2] | Ω [10^3 s^{-1}] | $T/ W $ | $\mathcal{M}/ W $ | ϵ_s | ϵ | GRV2 | GRV3 |
|---------|---------------------------------------|--|--|----------------------|---------------------------|-------------------------------------|---------------------------------------|---------|-------------------|--------------|------------|---------------------|---------------------|
| PP-Po12 | 7.408 | 2.917 | 8.409 | 1.427 | 14.34 | 1.278 | 0.000 | 0.00000 | 0.1326 | -0.0806 | -0.1986 | 4×10^{-11} | 3×10^{-9} |
| PO-Po12 | 5.898 | 2.324 | 7.077 | 1.427 | 16.35 | 1.549 | 3.969 | 0.03200 | 0.1056 | 0.1521 | -0.0684 | 1×10^{-10} | 2×10^{-10} |
| OO-Po12 | 3.264 | 1.393 | 5.470 | 1.424 | 19.05 | 1.971 | 5.050 | 0.07136 | 0.0422 | 0.5861 | 0.0856 | 7×10^{-7} | 4×10^{-6} |
| PP-APR | 8.046 | 3.597 | 6.036 | 1.438 | 13.58 | 1.136 | 0.000 | 0.00000 | 0.1754 | -0.1176 | -0.3045 | 5×10^{-7} | 4×10^{-7} |
| PO-APR | 7.361 | 3.255 | 5.861 | 1.437 | 14.64 | 1.247 | 4.219 | 0.02671 | 0.1494 | 0.0703 | -0.1622 | 2×10^{-6} | 1×10^{-6} |
| OO-APR | 5.548 | 2.551 | 5.493 | 1.432 | 16.31 | 1.431 | 6.004 | 0.06276 | 0.0878 | 0.4591 | 0.0072 | 2×10^{-6} | 3×10^{-6} |

the magnetisation is sufficiently strong. Although we have truncated the solution space toward high magnetisations, the minimum quadrupole distortion of $\epsilon = -0.6127$, which corresponds to the strongest prolate deformation of our sample and has been obtained for the nonrotating model at the magnetisation truncation limit, exceeds considerably the quadrupole distortion $\epsilon = 0.1537$ of the unmagnetised mass-shedding model rotating at $\Omega = 5.205 \times 10^3 \text{ s}^{-1}$ with $T/|W| = 0.09380$. This significant difference can be explained by the large ratio $\mathcal{M}/|W| = 0.2448$ of the magnetised model. Since no mass-shedding limit has been encountered in the nonrotating magnetised case, $\mathcal{M}/|W|$ can possibly attain arbitrarily high values and accordingly, the quadrupole distortion ϵ can, in principle, grow without bounds, too. We leave the assessment of this conjecture to a subsequent work.

We also note that whereas all mass-shedding models exhibit an oblate surface deformation for which $\epsilon_s > 0$, only rapidly rotating mass-shedding models with $\Omega \gtrsim 4.5 \times 10^3 \text{ s}^{-1}$ show a positive quadrupole distortion with $\epsilon > 0$. On the other hand, all mass-shedding models rotating at lower angular velocities actually possess a prolate matter distribution and $\epsilon < 0$ which, moreover, seems to grow without bounds for increasing magnetisation like in the nonrotating case. Altogether, Figs. 9 and 10 reveal that the neutral lines $\epsilon_s = 0$ and $\epsilon = 0$ differ significantly, suggesting the division of the space of solutions of magnetised and rotating models into three classes: (1) models for which apparent shape and distortion of the matter distribution are both prolate, thus with $\epsilon_s < 0$ and $\epsilon < 0$, which we label PP for prolate-prolate; (2) models for which the apparent shape is oblate and the distortion of the matter distribution is prolate, thus with $\epsilon_s > 0$ and $\epsilon < 0$, which we label PO for prolate-oblate; (3) models for which apparent shape and distortion of the matter distribution are both oblate, thus with $\epsilon_s > 0$ and $\epsilon > 0$, which we label OO for oblate-oblate. As a result, in contrast with the results of Kiuchi & Yoshida (2008), rotating models with a strong toroidal magnetic field do not necessarily exhibit a negative quadrupole distortion ϵ [cf. discussion in Sect. 2 and Fig. 1].

Representative models for each of the three classes located at the maximum field-strength limit have been presented in Sect. 5, namely model PP-Po12, the nonrotating configuration with a prolate apparent shape and a prolate matter distribution, and earlier in this Section, namely model PO-Po12, with a prolate apparent shape and an oblate matter distribution, and model OO-Po12 with an oblate shape and an oblate matter distribution. Within Figs. 9 and 10, their positions in the lower and upper parts of the solution space have been marked by red dots along the line of maximum

magnetic-field strength related to $\langle B^2 \rangle^{1/2}$. Note that no model exists for which the apparent shape is prolate and the distortion of the matter distribution oblate, i.e. $\epsilon_s < 0$ and $\epsilon > 0$; therefore, because of the different nature of the forces caused by a toroidal magnetic field and rotation, a class OP does not exist. While magnetic and centrifugal forces distort the matter distribution at a comparable level with respect to the involved amounts of magnetic and kinetic energy, the magnetic potential is confined and does not act on the surface of the star directly through Eq. (53). Therefore, already in the magnetised and nonrotating case, the surface deformation is always smaller than the quadrupole distortion. Moreover, since centrifugal forces act more efficiently at large distances from the rotation axis, their influence on the surface of the star can be significant, and indeed the value of $\epsilon_s = 0.7242$ obtained at the unmagnetised mass-shedding limit is considerably larger (in absolute terms) than the value obtained for the nonrotating model at the upper magnetisation limit of $\epsilon_s = -0.1369$; the opposite is true when considering the quadrupole distortion with respective values of $\epsilon = -0.6127$ and $\epsilon = 0.1537$.

In order to assess the general validity of our results obtained in the rotating case for the analytic Po12 EOS, we have compared the two rotating models PO-Po12 and OO-Po12 with the corresponding models PO-APR and OO-APR, built with the APR EOS for identical values of the $T/|W|$ ratio at the unmagnetised limit, i.e. $T/|W| = 0.03$ and $T/|W| = 0.07$. The physical properties of all models are listed in Table 4, where it is clear that the effects of rotation are less pronounced for the two APR models because of the stiffer nature of the APR EOS. The APR models admit a higher maximum value of $T/|W| = 0.1052$ at the unmagnetised mass-shedding limit, which should be compared with the corresponding $T/|W| = 0.09380$ for the softer Po12 EOS. Moreover, as discussed in Sect. 5, the APR EOS reference model supports a higher maximum field strength when compared to the Po12 EOS one, which causes magnetic effects to be stronger for the two models PO-APR and OO-APR.

The toroidal magnetic-field strength and the baryon number density for the PO-APR and OO-APR models are reported in Fig. 11, which shows that the matter distributions are less condensed (the EOS is stiffer) and the peaks of the magnetic-field strength have moved slightly outward. Their prolate deformation appears more pronounced in agreement with the higher ratio $\mathcal{M}/|W|$, and the outer crust is easily discernible because the magnetic field is essentially absent from this low density region. The ratio $T/|W|$ for models PO-APR and OO-APR is smaller than that of their unmag-

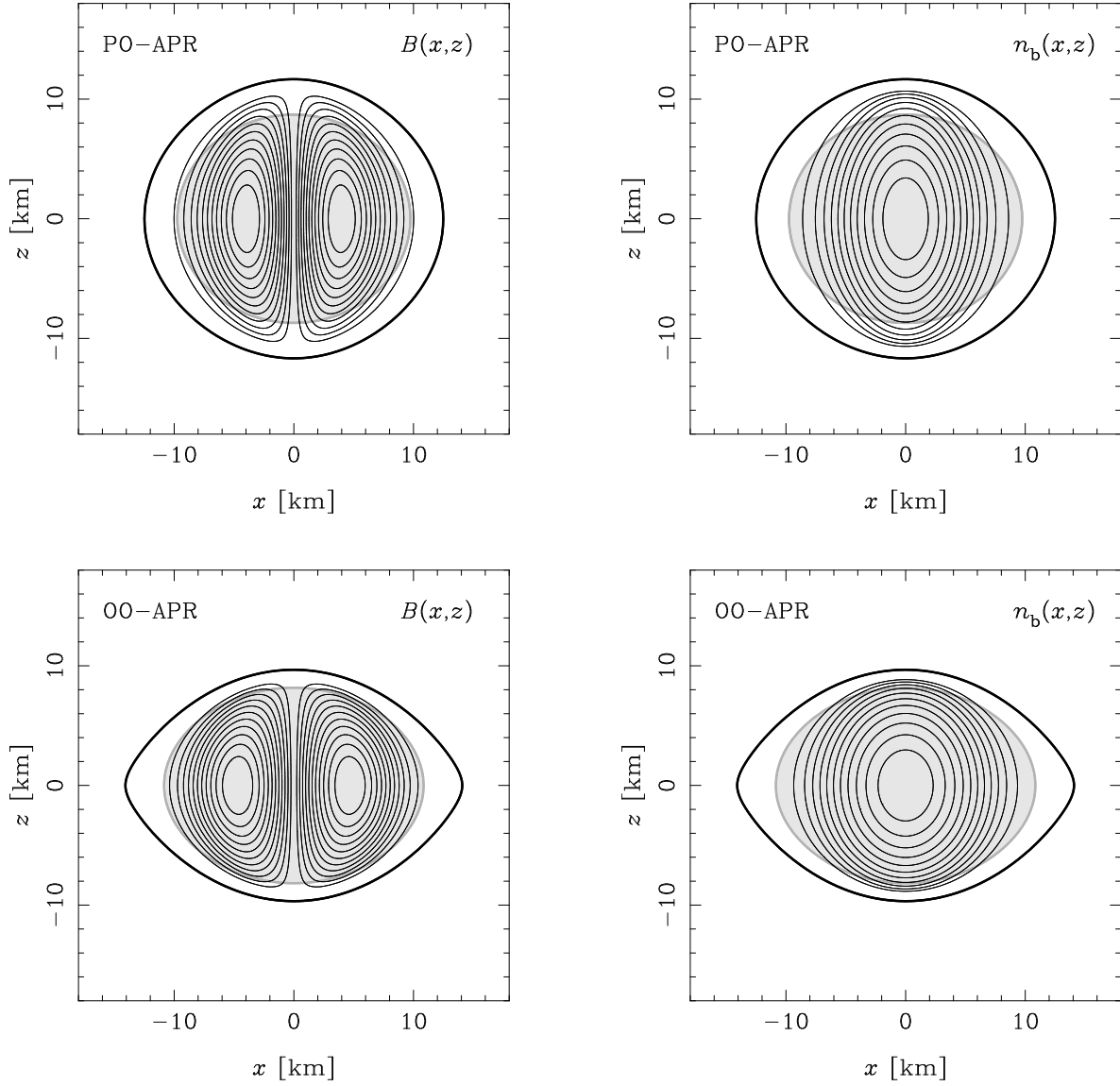


Figure 11. Isocontours of magnetic-field strength (left panel) and baryon number density (right panel) in the (x, z) plane of the PO-APR and OO-APR models of a star built with the APR EOS with a gravitational mass of $M = 1.400 M_\odot$ in the unmagnetised and nonrotating case which is now rotating at $\Omega = 4.219 \times 10^3 \text{ s}^{-1}$ (top) and $\Omega = 6.004 \times 10^3 \text{ s}^{-1}$ (bottom) respectively. The gray disc indicates the dimensions of the unmagnetised reference model. Physical properties of models PO-APR and OO-APR are listed in Table 4.

Table 5. Static reference models without magnetic field and with a gravitational mass of $M = 1.400 M_\odot$. $n_{b,c}$ is the central baryon number density [0.1 fm^{-3}], M_b the baryon mass, R_{circ} the circumferential radius, I the moment of inertia, b_B the magnetic distortion coefficient defined in Eq. (73), b_Ω the rotational distortion coefficient defined in Eq. (73), c_B the magnetic distortion coefficient defined in Eq. (73), c_Ω the rotational distortion coefficient defined in Eq. (73), and GRV2/GRV3 the estimates of the global error of respective models based on the relativistic virial identities introduced in Sect. 4.3.

| EOS | $n_{b,c}$ [0.1 fm^{-3}] | M_b [M_\odot] | R_{circ} [km] | I [10^{38} kg m^2] | b_B | b_Ω | c_B | c_Ω | GRV2 | GRV3 |
|--------|--|------------------------|---------------------------|-------------------------------------|------------------------|------------------------|------------------------|------------------------|---------------------|---------------------|
| Pol2 | 7.942 | 1.523 | 12.00 | 1.280 | 5.860×10^{-7} | 6.137×10^{-9} | 8.338×10^{-7} | 2.456×10^{-9} | 4×10^{-13} | 3×10^{-12} |
| APR | 5.538 | 1.553 | 11.34 | 1.306 | 6.545×10^{-7} | 5.579×10^{-9} | 7.922×10^{-7} | 2.481×10^{-9} | 6×10^{-5} | 8×10^{-5} |
| BBB2 | 6.368 | 1.555 | 11.13 | 1.256 | 5.809×10^{-7} | 5.229×10^{-9} | 6.989×10^{-7} | 2.282×10^{-9} | 6×10^{-5} | 8×10^{-5} |
| BN1H1 | 5.018 | 1.529 | 12.90 | 1.590 | 1.137×10^{-6} | 8.215×10^{-9} | 1.547×10^{-6} | 3.845×10^{-9} | 5×10^{-6} | 3×10^{-6} |
| BPAL12 | 11.88 | 1.549 | 10.06 | 0.971 | 2.619×10^{-7} | 3.528×10^{-9} | 3.178×10^{-7} | 1.267×10^{-9} | 2×10^{-5} | 3×10^{-5} |
| FPS | 6.949 | 1.559 | 10.85 | 1.200 | 4.912×10^{-7} | 4.821×10^{-9} | 5.798×10^{-7} | 2.076×10^{-9} | 5×10^{-5} | 7×10^{-5} |
| GNH3 | 3.654 | 1.512 | 14.20 | 1.814 | 1.577×10^{-6} | 1.078×10^{-8} | 2.362×10^{-6} | 5.132×10^{-9} | 1×10^{-4} | 1×10^{-4} |
| SLy4 | 5.376 | 1.546 | 11.72 | 1.367 | 7.422×10^{-7} | 6.141×10^{-9} | 9.310×10^{-7} | 2.756×10^{-9} | 9×10^{-5} | 1×10^{-4} |

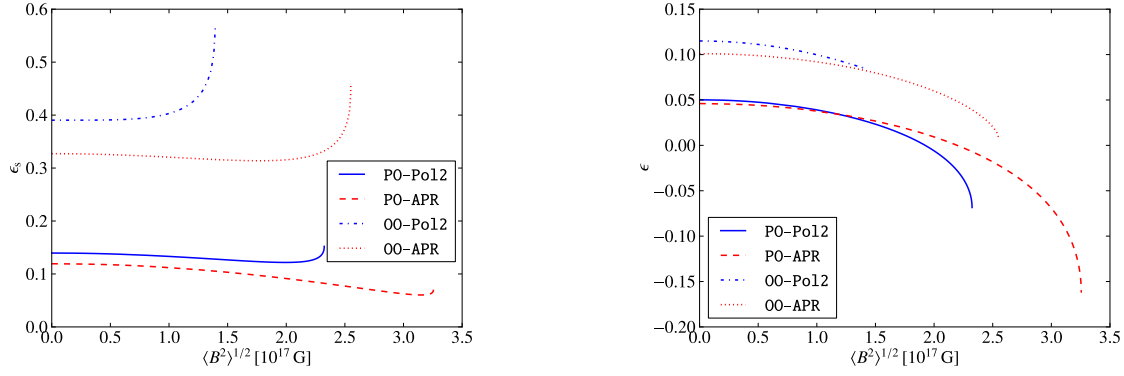


Figure 12. Surface deformation ϵ_s (left panel) and quadrupole distortion ϵ (right panel) for rotating models built with the Po12 EOS and the APR EOS as a function of the mean square magnetic-field strength $\langle B^2 \rangle$ from the unmagnetised limit up to the maximum field strength models PO-Po12 and PO-APR as well as OO-Po12 and OO-APR. The angular velocities are chosen such that $T/|W| = 0.03$ and $T/|W| = 0.07$ respectively in the unmagnetised case.

netised counterparts, in agreement with their smaller momenta of inertia. On the contrary, models PO-Po12 and OO-Po12 are already located in the region of increasing momenta of inertia and show ratios $T/|W| = 0.03200$ and $T/|W| = 0.07119$, which are larger than those of the unmagnetised models rotating at the same angular velocities Ω .

Finally, Fig. 12 compares the dependence of ϵ_s and ϵ on the magnetisation levels for the four reference rotating models (cf. Fig. 5, where the comparison was made for the nonrotating models PP-Po12 and PP-APR). Clearly, there is a good qualitative agreement between the two EOSs with differences that are due mostly to the higher maximum magnetic-field strength and the higher maximum value of $T/|W|$ supported by models PO-APR and OO-APR. Note that model OO-Po12 is so close to the mass shedding-limit that it is the only one for which models rotating at the same angular velocity Ω show increasing ϵ_s from the unmagnetised limit on. While all sequences in the left panel of Fig. 12 maintain an oblate shape, those associated with models PO-Po12 and PO-APR show a transition from an oblate matter distribution to a prolate one (right panel of Fig. 12).

7 DISTORTION COEFFICIENTS

Despite the complex behaviour shown by the equilibrium models when both the magnetic-field strength and the rotation are varied, it is possible to express such a behaviour through a very simple algebraic expression. This was pointed out already by Wentzel (1960) and by Ostriker & Gunn (1969), who have considered this issue in earlier Newtonian studies and have suggested to parametrize the quadrupole distortion ϵ_{Newt} induced by a toroidal magnetic field and by rotation in a self-gravitating incompressible fluid respectively as

$$\epsilon_{\text{Newt}} = \epsilon_B + \epsilon_\Omega = -a_B \frac{\mathcal{M}}{|W|} + a_\Omega \frac{T}{|W|}, \quad (72)$$

where $a_B = a_\Omega = 3.750$. This approximation was adopted also by Cutler (2002) in order to derive an estimate for the quadrupole distortion of neutron stars, within a Newtonian framework. Since neutron stars are highly relativistic objects, we next consider whether an expression similar to Eq. (72) can be derived in a relativistic regime and the quantitative differences that then emerge with respect to a Newtonian treatment.

We start by recalling that already in Sect. 6 we have remarked how the surface deformation ϵ_s and the quadrupole distortion ϵ for highly magnetised and rapidly rotating models exhibit an almost linear dependence on Ω^2 and on $\langle B^2 \rangle$. As a result, we can express these quantities in terms of “deformation coefficients”

$$\epsilon_s = -b_B \langle B_{15}^2 \rangle + b_\Omega \Omega^2, \quad \epsilon = -c_B \langle B_{15}^2 \rangle + c_\Omega \Omega^2, \quad (73)$$

where B_{15} expresses the magnetic-field strength in units of 10^{15} G and Ω is expressed in s^{-1} . The distortion coefficients b_B, b_Ω for the surface deformation ϵ_s and the coefficients c_B, c_Ω for the quadrupole distortion ϵ can be easily computed through the directional derivatives along the coordinate axes of Ω^2 and $\langle B^2 \rangle$ and are collected in Table 5 besides the basic properties of the unperturbed models for all of the EOSs considered. The importance of these distortion coefficients is that they provide all the information needed to compute the resulting values of ϵ_s and of ϵ by simply inserting appropriate values for the angular velocity Ω and for the mean magnetic-field strength $\langle B_{15}^2 \rangle^{1/2}$ in Eq. (73). In addition, the approximate expressions of Eq. (73) can cover a very large portion of the physically-realistic space of parameters and, for example, in the case of the Po12 EOS the phenomenological relations yield relative errors $\lesssim 8\%$ up to values of $\langle B^2 \rangle^{1/2} = 1 \times 10^{17}$ G and angular velocities of $\Omega = 2 \times 10^3 \text{ s}^{-1}$, which largely cover all known magnetars.

We note that the quadratic dependence expressed by Eq. (73) applies only to old and cold neutron stars *without* a superconducting proton phase, where the latter is expected to be suppressed for very strong magnetic fields above the critical one, i.e. for $\langle B \rangle > B_{c1} \approx 1 \times 10^{15}$ G. On the other hand, for magnetic field strengths of $\langle B \rangle < B_{c1}$, superconductivity is possible and the magnetic field is confined to flux tubes of strength $B_{c1} \approx 1 \times 10^{15}$ G, which enlarge the anisotropic part of the average electromagnetic stress tensor (Jones 1975; Easson & Pethick 1977), leading to a modification of the magnetic forces. As a result, for magnetised models with $\langle B \rangle < 10^{15}$ G, a *linear* dependence of the matter distortion on the average magnetic-field strength is expected and Eq. (73) has to be modified taking the alternate form

$$\epsilon_s = -b_B \langle B_{15} \rangle + b_\Omega \Omega^2, \quad \epsilon = -c_B \langle B_{15} \rangle + c_\Omega \Omega^2, \quad (74)$$

where the coefficients in Eq. (74) are the same as those in Eq. (73).

Figure 13 offers a graphical representation of the distortion coefficients for the surface deformation (left panel) and for the quadrupole distortion (right panel). The coefficients b_B and c_B

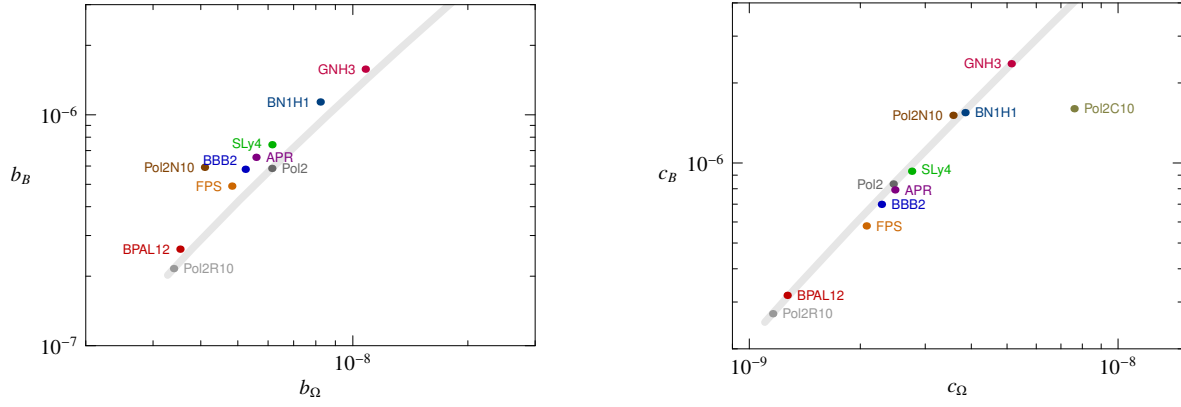


Figure 13. Distortion coefficients b_B and b_Ω for ϵ_s (left panel) as well as c_B and c_Ω for ϵ (right panel) derived in the linear regime by perturbing a nonrotating and unmagnetised star with a gravitational mass of $M = 1.400 M_\odot$.

as well as b_Ω and c_Ω are computed for different EOSs and using the reference nonrotating models with a gravitational mass of $M = 1.400 M_\odot$. Also shown as a gray-shaded band are the distortion coefficients of nonrotating models with a Pol2 EOS having the same gravitational mass, but where the polytropic constant is varied to obtain different circumferential radii R_{circ} (these have therefore $R_{\text{circ}} \geq 9.891$ km). The influence of the different EOSs is in fact most easily followed through the associated circumferential radius R_{circ} , which had already turned out to be a crucial quantity for the maximum field strength models presented in Sect. 5. As we explain in Appendix A, using basic scaling considerations, the magnetic distortion coefficients exhibit a dependence of the type $b_B, c_B \propto R_{\text{circ}}^4$, whereas the rotational distortion coefficients exhibit a dependence of the type $b_\Omega, c_\Omega \propto R_{\text{circ}}^3$.

Also shown for comparison in Fig. 13 are the Newtonian reference model from Cutler (2002), labelled Pol2C10, and its numerical equivalent as computed with our code in the Newtonian limit, labelled as Pol2N10⁶. Note that both Newtonian models have similar values of c_B and that the Pol2N10 data point is rather close to the reference band of relativistic Pol2 EOS models. However, the rotational distortion coefficient c_Ω reported in Cutler (2002) exceeds the correct Newtonian one of model Pol2N10 by almost a factor of two. Furthermore, both data points largely overestimate the correct relativistic result obtained for model Pol2R10 which is about a factor of four smaller and located at the lower end of the relativistic Pol2 EOS. This simple example highlights therefore how a Newtonian treatment is inadequate for the determination of realistic distortion coefficients for real neutron stars.

8 CONCLUSIONS

We have computed models of rotating relativistic stars with a toroidal magnetic field under the assumption that the matter is a single-constituent perfect fluid described by a one-parameter equation of state and behaves as a perfect conductor subject to the laws of ideal magnetohydrodynamics. We have investigated the combined effects of a toroidal magnetic field and rotation on the apparent shape and on the internal matter distribution, focussing in particular on the quadrupole distortion, as this is the relevant

quantity for the gravitational-wave emission. Models of maximum field strength have been computed for a sample of eight different nuclear-matter equations of state, together with the surface deformation and the quadrupole distortion.

We have found that nonrotating models appear to admit arbitrary levels of magnetisation accompanied by a seemingly unlimited growth of size and quadrupole distortion. In particular, we have been able to compute a highly magnetised model for the Pol2 EOS with a baryon mass of $M_b = 1.680 M_\odot$, whose circumferential radius of $R_{\text{circ}} = 14.30$ km in the unmagnetised case, inflates to $R_{\text{circ}} = 101.5$ km for an average magnetic field of $\langle B \rangle = 0.1461 \times 10^{17}$ G. These results should be contrasted with those of Kiuchi & Yoshida (2008), who reported a loss of convergence for this model at a moderate level of magnetisation and corresponding to a value of merely $R_{\text{circ}} = 28.85$ km.

When considering rotating models we have instead found that the increase in equatorial size introduced by the toroidal magnetic field reduces the frequency at which mass-shedding would otherwise appear in unmagnetised models. Overall, the full space of solutions can be split up into three distinct classes for which the surface distortion and the quadrupole distortion are either prolate and prolate, oblate and prolate or oblate and oblate, respectively.

We have also determined the relativistic distortion coefficients whose absolute value depends mainly on the radius of the star for all the EOSs considered. Using such coefficients it is possible to compute the surface deformation and the quadrupole distortion by means of a simple algebraic expression which is effective for all magnetisations and rotation rates of known magnetars. Finally, a comparison with the corresponding Newtonian distortion coefficients has shown that the latter overestimate the quadrupole distortion induced by the toroidal magnetic field by about a factor of five and the one induced by rotation by about a factor of four. Hence, they are inadequate for strongly-relativistic objects like neutron stars.

The results presented here relative to equilibrium configurations provide the first basic steps to explore the stability properties of magnetised stars, whose analysis in full general relativity has recently seen a spur of activity (Kiuchi et al. 2011; Lasky et al. 2011; Cioffi et al. 2011; Zink et al. 2012; Lasky et al. 2012; Cioffi & Rezzolla 2012). We will investigate the stability properties of our models in a forthcoming future work.

⁶ Only the quadrupole distortion coefficients c_B and c_Ω for model Pol2C10 were considered by Cutler (2002).

ACKNOWLEDGEMENTS

We thank Eric Hirschmann for useful discussions. This work was supported in part by the DFG grant SFB/Transregio 7. JF gratefully acknowledges financial support from the Daimler und Benz Stiftung.

REFERENCES

- Akmal A., Pandharipande V. R., Ravenhall D. G., 1998, *Phys. Rev. C*, 58, 1804
- Balberg S., Gal A., 1997, *Nuclear Physics A*, 625, 435
- Baldo M., Bombaci I., Burgio G. F., 1997, *Astron. Astrophys.*, 328, 274
- Bardeen J. M., Piran T., 1983, *Phys. Rep.*, 96, 205
- Bocquet M., Gourgoulhon E., Novak J., 1995, *Astron. Astrophys.*, 301, 757
- Bombaci I., 1995, in Bombaci I., Bonaccorso A., Fabrocini A., eds, *Perspectives on Theoretical Nuclear Physics* p. 223
- Bonanno A., Rezzolla L., Urpin V., 2003, *Astron. Astrophys.*, 410, L33
- Bonazzola S., 1973, *Astrophys. J.*, 182, 335
- Bonazzola S., Gourgoulhon E., 1994, *Classical and Quantum Gravity*, 11, 1775
- Bonazzola S., Gourgoulhon E., 1996, *Astron. Astrophys.*, 312, 675
- Bonazzola S., Gourgoulhon E., Marck J. A., 1998, *Phys. Rev. D*, 58, 104020
- Bonazzola S., Gourgoulhon E., Salgado M., Marck J.-A., 1993, *Astron. Astrophys.*, 278, 421
- Bonazzola S., Haensel P., 1993, (unpublished)
- Cardall C. Y., Prakash M., Lattimer J. M., 2001, *Astrophys. J.*, 554, 322
- Carter B., 1970, *Communications in Mathematical Physics*, 17, 233
- Carter B., 1973, in DeWitt C., DeWitt B. S., eds, *Black Holes - Les Houches 1972 Stationary-axisymmetry, circularity, and the papapetrou theorem*. pp 159–166
- Cioffi R., Ferrari V., Gualtieri L., 2010, *Mon. Not. Roy. Astron. Soc.*, 406, 2540
- Cioffi R., Ferrari V., Gualtieri L., Pons J. A., 2009, *Mon. Not. Roy. Astron. Soc.*, 397, 913
- Cioffi R., Lander S. K., Manca G. M., Rezzolla L., 2011, *Astrophys. J. Lett.*, 736, L6
- Cioffi R., Rezzolla L., 2012, *ArXiv e-prints*
- Colaiuda A., Ferrari V., Gualtieri L., Pons J. A., 2008, *Mon. Not. Roy. Astron. Soc.*, 385, 2080
- Cutler C., 2002, *Phys. Rev. D*, 66, 084025
- Das M. K., Tandon J. S., 1977, *Astrophysics and Space Science*, 49, 277
- Douchin F., Haensel P., 2001, *Astron. Astrophys.*, 380, 151
- Duncan R. C., Thompson C., 1992, *Astrophys. J. Lett.*, 392, L9
- Easson I., Pethick C. J., 1977, *Phys. Rev. D*, 16, 275
- Friebe J., Rezzolla L., 2007, *Rotating neutron star models with a toroidal magnetic field*, Talk at SFB/TR7 Video Seminar, <http://www.sfb.tpi.uni-jena.de/VideoSeminar/.../Files/20070618-friebe.pdf>
- Fujisawa K., Yoshida S., Eriguchi Y., 2012, *Mon. Not. Roy. Astron. Soc.*, 422, 434
- Glendenning N. K., 1985, *Astrophys. J.*, 293, 470
- Gourgoulhon E., ed. 2012, *3+1 Formalism in General Relativity* Vol. 846 of *Lecture Notes in Physics*, Berlin Springer Verlag
- Gourgoulhon E., Bonazzola S., 1993, *Phys. Rev. D*, 48, 2635
- Gourgoulhon E., Bonazzola S., 1994, *Classical and Quantum Gravity*, 11, 443
- Gourgoulhon E., Haensel P., Livine R., Paluch E., Bonazzola S., Marck J., 1999, *Astron. Astrophys.*, 349, 851
- Gourgoulhon E., Markakis C., Uryū K., Eriguchi Y., 2011, *Phys. Rev. D*, 83, 104007
- Gualtieri L., Cioffi R., Ferrari V., 2011, *Classical and Quantum Gravity*, 28, 114014
- Haskell B., Samuelsson L., Glampedakis K., Andersson N., 2008, *Mon. Not. Roy. Astron. Soc.*, 385, 531
- Haskell B., Samuelsson L., Glampedakis K., Andersson N., 2009, *Mon. Not. Roy. Astron. Soc.*, 394, 1711
- Ioka K., Sasaki M., 2003, *Phys. Rev. D*, 67, 124026
- Ioka K., Sasaki M., 2004, *Astrophys. J.*, 600, 296
- Jones P. B., 1975, *Ap&SS*, 33, 215
- Kiuchi K., Kotake K., Yoshida S., 2009, *Astrophys. J.*, 698, 541
- Kiuchi K., Yoshida S., 2008, *Phys. Rev. D*, 78, 044045
- Kiuchi K., Yoshida S., Shibata M., 2011, *Astron. Astrophys.*, 532, A30
- Lai D., Rasio F. A., Shapiro S. L., 1993, *Astrophys. J. Suppl.*, 88, 205
- Lander S. K., Jones D. I., 2009, *Mon. Not. Roy. Astron. Soc.*, 395, 2162
- Lasky P. D., Zink B., Kokkotas K. D., 2012, *ArXiv e-prints*
- Lasky P. D., Zink B., Kokkotas K. D., Glampedakis K., 2011, *Astrophys. J. Lett.*, 735, L20
- Miketinac M. J., 1973, *Equilibrium Structure of Polytropes with Toroidal Magnetic Fields*
- Naso L., Rezzolla L., Bonanno A., Paternò L., 2008, *Astron. Astrophys.*, 479, 167
- Nozawa T., Stergioulas N., Gourgoulhon E., Eriguchi Y., 1998, *Astron. Astrophys. Suppl.*, 132, 431
- Oron A., 2002, *Phys. Rev. D*, 66, 023006
- Ostriker J. P., Gunn J. E., 1969, *Astrophys. J.*, 157, 1395
- Pandharipande V., Ravenhall D., 1989, *Hot Nuclear Matter, in Nuclear Matter and Heavy Ion Collisions*. Vol. B205, NATO ADS Ser.
- Salgado M., Bonazzola S., Gourgoulhon E., Haensel P., 1994, *Astron. Astrophys.*, 291, 155
- Sinha N. K., 1968, *Australian Journal of Physics*, 21, 283
- Smarr L., York Jr. J. W., 1978, *Phys. Rev. D*, 17, 2529
- Sood N. K., Trehan S. K., 1972, *Astrophysics and Space Science*, 16, 451
- Stella L., Dall’Osso S., Israel G. L., Vecchio A., 2005, *Astrophys. J. Lett.*, 634, L165
- Swesty F., 1996, *Journal of Computational Physics*, 127, 118
- Thompson C., Duncan R. C., 1996, *Astrophys. J.*, 473, 322
- Thorne K. S., 1980, *Reviews of Modern Physics*, 52, 299
- Tomimura Y., Eriguchi Y., 2005, *Mon. Not. Roy. Astron. Soc.*, 359, 1117
- Villain L., Pons J. A., Cerdá-Durán P., Gourgoulhon E., 2004, *Astron. Astrophys.*, 418, 283
- Wentzel D. G., 1960, *Astrophys. J. Suppl.*, 5, 187
- Yasutake N., Kiuchi K., Kotake K., 2010, *Mon. Not. Roy. Astron. Soc.*, 401, 2101
- Yasutake N., Maruyama T., Tatsumi T., 2011, *Journal of Physics Conference Series*, 312, 042027
- Yoshida S., Kiuchi K., Shibata M., 2012, *ArXiv e-prints*
- Yoshida S., Yoshida S., Eriguchi Y., 2006, *Astrophys. J.*, 651, 462
- Zink B., Lasky P. D., Kokkotas K. D., 2012, *Phys. Rev. D*, 85, 024030

APPENDIX A: ASSESSMENT OF RESULTS BY CUTLER (2002)

As anticipated in Sect. 7, earlier Newtonian studies have suggested to express the quadrupole distortion ϵ_{Newt} induced in a self-gravitating incompressible fluid by a toroidal magnetic field and by rotation respectively as function of the total magnetic energy \mathcal{M} , of the kinetic energy T , and of the potential energy W , namely through Eq. (72) (Wentzel 1960; Ostriker & Gunn 1969). For a spherical star built with a polytropic EOS with $\gamma = 2$ it is easy to estimate that

$$T = \frac{1}{5}\kappa_1 MR^2\Omega^2, \quad W = -\frac{3}{4}\frac{M^2}{R}, \quad (\text{A1})$$

where $\kappa_1 = 0.65345$ is a constant derived by Lai et al. (1993). As a result, the ratio of the kinetic to binding energy will scale as $T/|W| \propto R^3$. On the other hand, the total magnetic energy \mathcal{M} of the same body reads

$$\mathcal{M} = \frac{1}{8\pi} \int_V B^2 dV = \frac{4\pi}{3} R^3 \langle B^2 \rangle, \quad (\text{A2})$$

where $\langle B^2 \rangle$ denotes the mean square average of the magnetic-field strength B inside the star. It then follows that $\mathcal{M}/|W| \propto R^4$. Eventually, the total distortion ϵ can be expressed in terms of mean magnetic-field strength $\langle B^2 \rangle^{1/2}$ and angular velocity Ω , namely [cf. Eq. (73)]

$$\epsilon_{\text{Newt}} = \epsilon_B + \epsilon_\Omega = -c_B \langle B_{15}^2 \rangle + c_\Omega \Omega^2. \quad (\text{A3})$$

For a Newtonian model with $M = 1.400 M_\odot$ and a radius of $R = 10.00$ km, Cutler (2002) has computed c_B according to Eqs. (A1) and (A2) and reported the distortion coefficients as

$$c_B = 1.600 \times 10^{-6}, \quad c_\Omega = 7.600 \times 10^{-9}. \quad (\text{A4})$$

However, if we use Eqs. (A1) and (A2) and adopt an identical model with $M = 1.400 M_\odot$ and $R = 10.00$ km, we obtain

$$c_B = 1.610 \times 10^{-6}, \quad c_\Omega = 3.516 \times 10^{-9}, \quad (\text{A5})$$

where $c_\Omega = 6.725 \times 10^{-9}$ for an incompressible fluid. Although the estimates for c_B agree reasonably well, our value for c_Ω is less than half the one quoted in Cutler (2002), which is instead close to the corresponding value for a homogeneous sphere. To validate our estimates, we have additionally computed the distortion coefficients with our numerical code in the Newtonian limit and obtained

$$c_B = 1.511 \times 10^{-6}, \quad c_\Omega = 3.569 \times 10^{-9}, \quad (\text{A6})$$

which agree well with the estimates from Eq. (A5). The remaining difference is due to the fact that $a_B = a_\Omega = 3.750$ only in the incompressible case and need to be corrected in the compressible one. After taking into account this EOS dependence, full agreement is achieved, as can be verified in Table A1, which provides a compilation of the different values for the coefficients c_B and c_Ω and where the coefficients a_B and a_Ω have been added when available.

Table A1. Distortion coefficients for a Newtonian star with $M = 1.400 M_\odot$ and $R = 10.00$ km for a polytropic EOS with $\gamma = 2$. For comparison, values for an incompressible model with the same properties are included.

| γ | a_B | a_Ω | c_B | c_Ω |
|------------|-------|------------|------------------------|------------------------|
| ∞^1 | 3.750 | 3.750 | 2.013×10^{-6} | 6.725×10^{-9} |
| 2^2 | 3.750 | 3.750 | 1.610×10^{-6} | 3.516×10^{-9} |
| 2^3 | 3.518 | 3.804 | 1.511×10^{-6} | 3.569×10^{-9} |
| 2^4 | — | — | 1.511×10^{-6} | 3.567×10^{-9} |
| 2^5 | 3.750 | — | 1.600×10^{-6} | 7.600×10^{-9} |

1. Distortion coefficients c_B and c_Ω according to Eq. (72). In the incompressible case, $T = I\Omega^2/2$ with $I = (2/5)MR^2$, and $W = -(3/5)M^2/R$.
2. As before but using Eqs. (A1) and (A2).
3. Distortion coefficients derived from the linear perturbation of a numerical Newtonian model.
4. Distortion coefficients from Haskell et al. (2008) revised by Haskell et al. (2009).
5. Distortion coefficients from Cutler (2002).